International journal
for science, technics and
innovations for the industry

MACHINES TECHNOLOGIES MATERIALS

YEAR XIX Issue 12 / 2025 ISSN PRINT 1313-0226
ISSN WEB 1314-507X



Published by
Scientific technical
Union of Mechanical Engineering

MACHINES. TECHNOLOGIES. MATERIALS

INTERNATIONAL SCIENTIFIC JOURNAL

ISSN PRINT 1313-0226, ISSN WEB 1314-507X, YEAR XIX, ISSUE 12 / 2025

INTERNATIONAL EDITORAL BORARD

EDITOR IN CHIEF:		
Georgi Popov	Technical University of Sofia	BG
MEMBERS:		
Abdrakhman Naizabekov	Rudny industrial institute	KZ
Ahmet H. Ertas	Bursa Technical University	TR
Albert Albers	Karlsruhe Institut of Technology	DE
Andrzej Golabczak	Lodz University of Technology	PL
Dimitar Karaivanov	University of Chemical Technology and Metallurgy, Sofia	BG
Dobre Runchev	Ss. Cyril and Methodius University in Skopje	NM
Emilia Abadjieva	Akita University	JP
Erdem Camurlu	Akdeniz University, Antalya	TR
Eugen Sheregii	University of Rzeszow	PL
Franz Haas	Graz University of Technology	AT
Galina Nicolcheva	Technical University of Sofia	BG
Gennadii Bagliuk	Institute for Problems of Materials Science NAS of Ukraine, Kiev	UA
Georgii Raab	Ufa State Aviation Technical University	RU
Gregory Gurevich	Shamoon College of Engeeniring, Ashdod	IL
Hiroyuki Moriyama	Tokai University, Hiratsuka	JP
Idilia Batchkova	University of Chemical Technology and Metallurgy, Sofia	BG
Iryna Charniak	National Academy of Science, Belarus	BY
Ivan Kralov	Technical University of Sofia	BG
Ivan Kuric	University of Zilina	SK
Iurie Melnic	Technical University of Moldova	
Jaroslaw Piatkowski	Silesian University of Technology	PL
Julieta Kaleicheva	Technical University of Sofia	BG
Katia Vutova	Institute of Electronics, Bulgarian Academy of Sciences	BG
Maria Nikolova	Angel Kanchev University of Ruse	BG
Natasa Naprstkova	Jan Evangelista Purkyne University in Usti nad Labem	CZ
Oana Dodun	Gheorghe Asachi Technical University of Iasi	RO
Ognyan Andreev	Technical University of Sofia	BG
Predrag Dasic	High Technical Mechanical School of Trstenik	RS
Rasa Kandrotaite	Kaunas University of Technology	LT
Raul Turmanidze	Georgian Technical University, Tbilisi	GE
Roumen Petrov	Ghent University	BE
Sergey Dobatkin	National University of Science and Technology "MISIS", Moscow	RU
Souren Mitra	Jadavpur University, Kolkata	IN
Svetlana Gubenko	National Metallurgical Academy of Ukraine, Dnipro	UA
Vedran Mrzljak	University of Rijeka	HR
Wu Kaiming	Wuhan University of Science and Technology	CN

TECHNICAL EDITORS:

M. Sc. Eng. Radoslav Daskalov,
M. Sc. Eng. Oleg Mihailov

All articles are published after peer review by two independent reviewers.

Scientific and technical union of mechanical engineering
108 R. S. Rakovski str., Sofia, Bulgaria
www.stumejournals.com, office@stumejournals.com

C O N T E N T S

MACHINES

Design of a Robotic-Based Multi-Packaging Machine
Oğulcan Sogut, Y.Yağız Simsek, M. Baris Yildiz, Yusuf Sahinoglu, Nesrin Sen, Onur Cimen, I. Etem Saklakoglu 452

Thermodynamic Modeling and Matlab-based Simulation of a Stirling Engine for Micro- Scale Power Generation
Ardit Gjeta, Spartak Poçari, Majlinda Alcani, Tauland Spahiu 456

Research on deformations of a flexible screw sectional working body
Volodymyr Bulgakov, Oleksandra Trokhaniak, Stanislav Kovalchuk, Olha Dubrovina 460

Investigation of the parameters of a curved channel of the confuser type
Viktor Trokhaniak 463

TECHNOLOGIES

Tribological Analysis of Plasma Spray Thermal Deposition on the Active Area of Harrow Discs
Corneliu Munteanu, Iurie Melnic, Bogdan Istrate, Marcelin Benchea, Constantin Zîrnescu, Vladimir Badiul 466

Application of single-point incremental forming with industrial robot arm to analyze the impact of system stiffness on forming precision
Kosma Knap, Konrad Perzynski, Lukasz Madej 470

Thermoeconomic Analysis of an Organic Rankine Cycle for LNG Cold Energy Utilization
Josip Grbac, Paolo Blecich, Mateo Kirinčić, Igor Bonefačić 472

MATERIALS

Optical and microstructural properties of hybrid sol–gel derived ZrO_2–Al_2O_3–Sm_2O_3 coatings on glass for photovoltaic applications
Shaban Uzun, Stancho Yordanov, Mariela Dimitrova, Vladimir Petkov, Tatyana Ivanova, Angel Velikov 476

Phenomena during liquid-phase assisted sintering in High-Entropy Ceramics with a Ni binder
Humeniak Mykola, Vedel Dmytro, Vronska Yuliia, Zatsarna Oleksandra, Taran Serhii, Stasiuk Oleksandr 479

Design of a Robotic-Based Multi-Packaging Machine

Oğulcan Sogut[1*], Y.Yağız Simsek[1], M. Baris Yildiz[1], Yusuf Sahinoglu[1], Nesrin Sen[1], Onur Cimen[1], I. Etem Saklakoglu[1-2]
KANSAN R&D Center, Izmir, Turkiye[1]
Ege University, Department of Mechanical Engineering, Izmir, Turkiye[2]
ogulcansogut@kansanmak.com

Abstract: *This study presents the comprehensive design and architectural modeling of a robotic-based multi-packaging machine developed for high-speed and high-precision packaging processes. The system integrates a Delta robot-based pick-and-place unit, advanced servo-controlled horizontal packaging modules, and a modular conveyor design engineered for multi-product stream transfer. This work investigates the core operational challenges, including product flow management, optimized grouping strategies, dynamic conveyor synchronization, coordination of multi-axis servo movements, and the system's overall operational efficiency. The results indicate that the developed system operates with high stability, achieves superior precision, and significantly enhances production throughput by providing automatic parameter optimization based on product variety, thereby aligning with modern Industry 4.0 requirements.*
Keywords*: ROBOTIC PACKAGING, DELTA ROBOT, MULTI-FEEDING, SERVO CONTROL, INDUSTRIAL AUTOMATION.*

1. Introduction

Packaging machinery constitutes one of the most critical and performance-demanding components of production lines in the Fast-Moving Consumer Goods (FMCG) industry, necessitating rigorous standards for speed, precision, and operational stability. Traditionally, mechanically driven packaging solutions are optimized for limited product types, which results in significant and often unavoidable downtime, costly adjustments, and material waste during format changeovers or speed variations [1].

1.1. Problem Statement and Motivation

The proliferation of Industry 4.0 principles and the growing market demand for customized, low-volume, high-mix production have rendered conventional rigid automation systems inefficient and non-adaptive. The critical technological gap lies in the inability of these traditional systems to seamlessly handle the simultaneous grouping of diverse products from multiple feeder lines into a single package, known as multi-packaging, without sacrificing cycle time or precision [2]. This scenario necessitates the development of flexible, high-speed, and intelligent packaging solutions capable of on-the-fly reconfigurability.

1.2. Research Objectives and Contribution

In response to this technological deficit, this study presents the comprehensive design, architectural modeling, and performance analysis of a high-speed robotic-based multi-packaging machine. This novel system addresses the limitations of conventional systems by integrating parallel kinematics with advanced motion control.

The primary contributions of this work are manifold:

i. Architecture Design: Developing a robust, modular mechanical architecture centered around a high-speed Delta robot pick-and-place system integrated with servo-controlled horizontal packaging modules.

ii. Advanced Synchronization: Establishing a precise, low-latency (<0.1 s) synchronization control loop for dynamic tracking and coordination between the high-speed robot, the modular feeding conveyors, and the downstream sealing jaws.

iii. Process Optimization: Investigating and validating novel product flow management and grouping strategies (e.g., 2-, 3-, and 4- unit grouping) that utilize automatic parameter optimization based on the specific product recipe to maximize Operational Equipment Effectiveness (OEE).

This article details the machine's robotic structure design, control architecture, product flow management, system synchronization, mechanical frame specifications, and quantitative performance analyses. The results demonstrate that the developed system achieves high stability and significantly enhances production efficiency by providing automated adaptability to product variety.

2. Literature Review

The imperative for high-speed, flexible, and versatile packaging solutions in the FMCG sector has driven significant research into advanced robotic systems. Traditional mechanically linked packaging systems often struggle with the requirements of low-volume, high-mix production and necessitate significant changeover times for format transitions, highlighting the operational limitations discussed by Wang et al. (2015) in the context of Cyber-Physical Systems (CPS) [17].

2.1. The Role of Parallel Kinematic Robots (PKRs)

The study of multi-packaging and high-speed picking systems consistently demonstrates the superiority of robotic platforms—particularly Parallel Kinematic Robots (PKRs)—over conventional mechanical architectures in terms of production flexibility and speed [1]. Among PKRs, the Delta robot configuration, originally developed by Clavel (1991), is overwhelmingly preferred in the packaging industry [2].

Its prevalence stems from its inherent design advantages:
• Exceptional Acceleration and Speed: Delta robots can achieve high acceleration capabilities (often up to 15 m/s^2) and high cycle rates, with some commercial models capable of executing over 300 picks per minute [3, 4].
• Low Moving Mass and High Stiffness: The parallel architecture ensures actuators are mounted on the base, minimizing moving inertia and maximizing the stiffness-to-weight ratio [5].
• Superior Positioning Accuracy: The closed-loop kinematics of the Delta mechanism provide very high precision and repeatability, typically within +/- 0.1mm or better, which is critical for precision alignment tasks [6].
• Compact Footprint: These robots can be mounted above the workspace, allowing for easy integration into existing or modular line designs [7].
These core advantages position Delta robots as the industry standard for demanding pick-and-place and sorting applications [8, 9].

2.2. Servo Control and System Synchronization

A central technological pillar enabling the high performance of modern packaging lines is the sophisticated coordination of multi-axis servo systems. The integration of high-speed robotics with continuous product flow necessitates precise conveyor tracking [10]. Kragic and Christensen (2002) pioneered the development of algorithms for intercepting moving objects, forming the foundation for modern tracking mode operations [10].

In the context of multi-packaging, the precise synchronization of

three main elements is paramount: the robot's end-effector, the product's moving coordinate on the conveyor, and the timing of the downstream packaging (sealing) module [11].

• Dynamic Coordinate Mapping: This involves receiving real-time speed and position feedback from the conveyor's encoder to dynamically adjust the robot's trajectory, a technique that significantly enhances picking efficiency [12].
• Multi-Axis Coordinated Motion: Contemporary packaging machines utilize networked servo drives (e.g., EtherCAT or PROFINET-based architectures) to ensure sub-millisecond synchronization between the robot controller, the feeding conveyor motors, and the servo-controlled sealing jaws [13, 14]. This precise coordination is essential for maintaining constant product pitch and achieving perfect sealing [15]. Research indicates that implementing such integrated servo-driven technology can improve overall line efficiency and cycle time by 20-40% compared to older mechanical cam-driven systems [16].

2.3. Flexibility and Industry 4.0

The design of a modular, robotic-based multi-packaging system aligns directly with the core tenets of Industry 4.0, which emphasizes decentralized control, real-time adaptability, and system interoperability [17]. The ability of the proposed system to handle various unit groups within a single machine demonstrates a high level of reconfigurability and flexibility, allowing manufacturers to rapidly switch between product recipes without extensive mechanical retooling [18]. This adaptability is crucial for achieving the "smart factory" ideal of customized, low-batch production [19]. Furthermore, the deployment of modular components and automated parameter optimization reduces both operational costs and the non-productive downtime associated with manual changeovers [20].

3. General System Design

The multi-packaging machine is engineered as a robust, modular system adhering to high industrial automation standards. The design philosophy centers on achieving maximal throughput and operational flexibility through the precise coordination of high-speed robotics and multi-axis servo technology.

3.1. Mechanical Structure and Modularity

The overall machine architecture is constructed from three primary, modular, and functionally distinct units:
Feeding Conveyor Modules: Responsible for delivering multiple product streams. They feature speed-controlled servo motors and integrated encoders for continuous, real-time positional feedback.

Delta Robot Pick-and-Place Unit: The high-speed core employing a 3-Degrees-of-Freedom (3-DOF) Delta mechanism for product singulation, grouping, and transfer.

Horizontal Form-Fill-Seal (HFFS) Packaging Module: Performs the final packaging operation, driven by synchronized servo controls, featuring servo-controlled jaw and disc assemblies for precise heat-sealing and cut-off.

The machine's structural integrity is secured by a robust carrier skeleton fabricated from AISI 304 stainless steel, ensuring compliance with food grade and hygiene standards (e.g., EHEDG guidelines). The developed multi-packaging machine's front, rear, and top general views are presented in Figures 1, 2, and 3, respectively

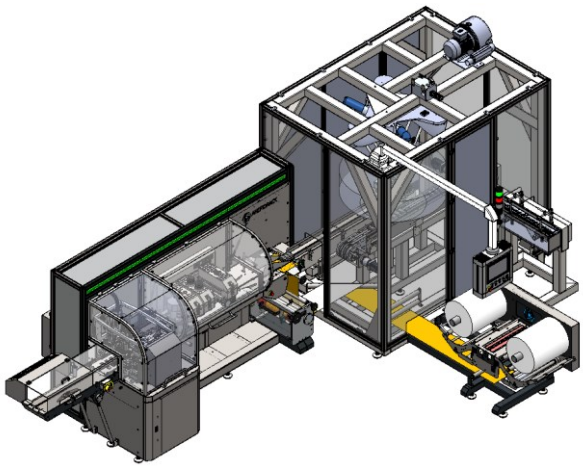


Figure 1: Front View of the Multi-Packaging Machine

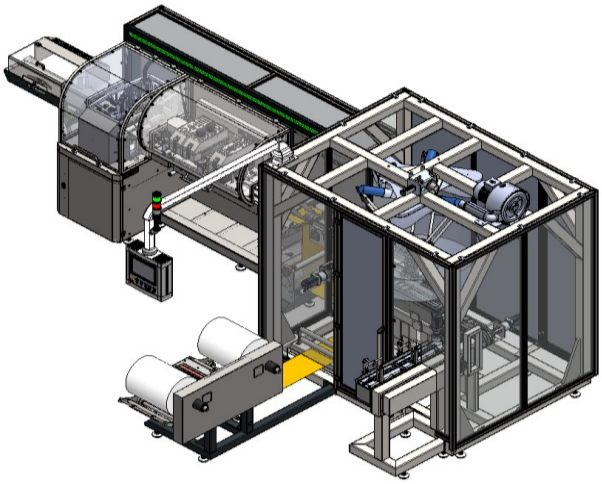


Figure 2: Rear View of the Multi-Packaging Machine

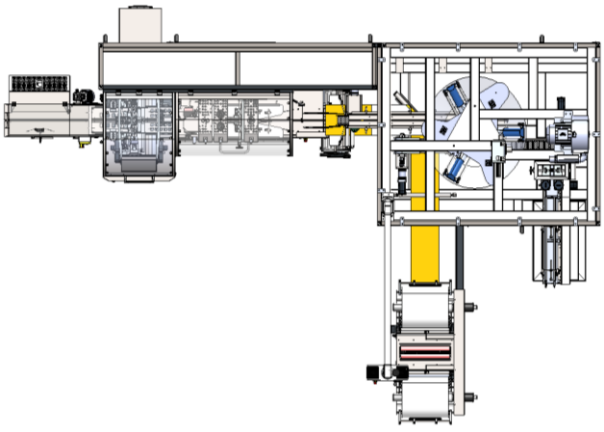


Figure 3: Top View of the Multi-Packaging Machine

3.2. Conveyor Tracking Algorithm and Synchronization Control

Achieving high-speed pick-and-place requires the seamless integration of the robot's motion with the continuously moving conveyor via a sophisticated real-time "Tracking Mode" algorithm. The robot controller dynamically calculates the necessary trajectory adjustments based on four critical data streams:

Table 1. Data streams for necessary trajectory adjustments

Data Stream	Function
Product x-y Coordinate	Defines the precise, instantaneous location of the target product
Conveyor Velocity (v)	Provides the instantaneous speed of the transport belt.
Product Arrival Time (t_a)	Predicts the time remaining until the product reaches the transfer zone
Packaging Jaw Synchronization Point (P_sync)	Defines the exact spatial coordinate for alignment with the sealing cycle.

4. Multi-Packaging Scenario and Grouping Strategy

The machine is capable of assembling and packaging multiple product groups simultaneously within a single wrapper, including: 2-Unit, 3-Unit, or 4-Unit Groups.

The operation is managed through a precise sequence: Product singulation > Robotic grouping > Product alignment > Servo jaw synchronization > Wrapper advancement and transfer. This high-level synchronization maximizes production throughput while accommodating high variability in packaging recipes.

5. Conclusion

The robotic-based multi-packaging machine developed and presented in this study represents a significant advancement in flexible industrial automation. By leveraging the dynamic capabilities of the Delta robot and the precision of multi-axis servo control, the system provides measurable improvements in both production efficiency and product quality stability across manufacturing lines.

5.1. Summary of Findings

The experimental and analytical results confirm the system's robust performance:

• Quality and Reliability: The high accuracy and repeatability ($\pm 0.1 \text{ mm}$) ensure correct grouping and damage-free transfer, increasing the consistency of packaging quality.

• Operational Efficiency: The integrated automatic grouping and synchronized transport capability drastically reduces manual intervention, resulting in shorter cycle times and a substantial increase in overall production speed.

• Flexibility and Adaptability: The robot-centric architecture allows the system to seamlessly accommodate variations in product size and form, confirming its suitability for modern flexible manufacturing requirements and enabling manufacturers to diversify their product offerings.

5.2. Strategic Impact and Future Work

The integration of a streamlined robotic system minimizes in-process waste and reduces the error rate, leading to a demonstrable reduction in overall manufacturing costs. These technical and economic gains collectively boost the operational efficiency of the enterprise and strengthen its market competitiveness.

In summation, the developed robotic-based multi-packaging machine is strategically positioned as a sustainable solution for modern industrial applications, delivering high efficiency, stable quality, low operating cost, and superior flexible manufacturing capabilities.

Future work will focus on incorporating advanced predictive maintenance routines using machine learning models trained on servo drive feedback data, and exploring the integration of collaborative robotics (Cobots) for complementary end-of-line secondary packaging tasks.

5. References

[1] Bogue, R. The role of robotics in food packaging. Industrial Robot: An International Journal, 45(2), 137–142, 2018.

[2] Clavel, R. Reduced inertia parallel robot. Proceedings of the 1991 IEEE International Conference on Robotics and Automation, 439–444, 1991.

[3] ABB Robotics. IRB 360 FlexPicker: The world's fastest picker. (Commercial specification cited for performance context).

[4] Zhao, Q., et al. A review of high-speed robot design and control methods for pick-and-place tasks. Journal of Automation and Control Engineering, 11(1), 12-25, 2023.

[5] Siciliano, B., et al. Robotics: Modelling, Planning and Control. Springer, 2009.

[6] Gao, H., et al. Precision analysis and optimization of a high-speed delta parallel robot. Mechanism and Machine Theory, 155, 104040, 2021.

[7] Hegazy, S. Comparative analysis of SCARA and Delta robot kinematics for packaging applications. International Journal of Advanced Robotic Systems, 17(5), 1-12, 2020.

[8] Johnson, D., and Wang, Q. Advances in soft grippers for delicate product handling in automated packaging. Packaging Technology and Science, 35(7), 541-558, 2022.

[9] Rovetta, S., and Zoppi, M. Robotic manipulation in the food industry: Challenges and opportunities. Journal of Food Engineering, 260, 109530, 2019.

[10] Kragic, D., and Christensen, H. I. Conveyor tracking for industrial pick-and-place operations. IEEE Transactions on Robotics and Automation, 18(6), 974–985, 2002.

[11] Chen, F., and Li, S. Real-time synchronization control strategy for robotic packaging lines under variable speed. Control Engineering Practice, 142, 105650, 2024.

[12] Lee, J., et al. Adaptive motion planning for high-speed pick-and-place with moving objects using machine vision. Robotics and Computer-Integrated Manufacturing, 80, 102430, 2023.

[13] Vogel-Heuser, B., and Hess, D. Industry 4.0—prerequisites and visions. IEEE Transactions on Automation Science and Engineering, 13(2), 411–413, 2016.

[14] LS Electric. Packaging Automation Solution: Integrated Servo and PLC Architecture. (Technical documentation cited for industry standard synchronization methods).

[15] Zhang, Y., and Liu, M. A highly synchronized motion control system for rotary-jaw flow wrappers. Mechatronics, 71, 102430, 2020.

[16] Schulze, L., and Müller, B. Performance evaluation of servo-driven versus mechanical packaging systems. International Journal of Manufacturing Technology and Management, 41(1), 115-135, 2023.

[17] Wang, L., Törngren, M., and Onori, M. Current status and advancement of cyber-physical systems in manufacturing. Journal of Manufacturing Systems, 37, 517–527, 2015.

[18] Tolio, T., et al. Design and management of smart and flexible production systems: A review. CIRP Annals—Manufacturing Technology, 66(2), 795–815, 2017.

[19] Brettel, M., et al. How virtualization, decentralization and network intelligence will change the manufacturing landscape. Procedia CIRP, 24, 111-118, 2014.

[20] Sadeghi, A., et al. Opportunities and challenges for adoption of robotics in packaging industry: A Review. IOSR Journal of Engineering, 14(1), 32-38, 2022.

Thermodynamic Modeling and Matlab-based Simulation of a Stirling Engine for Micro-Scale Power Generation

Ardit Gjeta [1], Spartak Poçari [2], Majlinda Alcani [3], Tauland Spahiu [4]
Energy Department, Mechanical Engineering Faculty, Polytechnic University of Tirana, Tirana, Albania [1, 2, 3, 4]
agjeta@fim.edu.al

Abstract: *The Stirling engine represents one of the most promising technologies for the efficient conversion of thermal energy into mechanical work, due to its ability to operate with almost any heat source and to achieve theoretical efficiencies approaching the Carnot cycle. This article aims to provide a detailed study of the Stirling cycle, the development of a mathematical model, numerical simulation using MATLAB and the analysis of the engine performance as a function of the main thermodynamic parameters, with special emphasis on applications in micro-power generation. A distinctive aspect of this study lies in the comprehensive treatment of the polynomial dependence of specific heat in all thermodynamic processes, enabling a more accurate representation of real gas behavior compared to idealized classical models. The mathematical model is formulated using the fundamental laws of thermodynamics and the ideal gas equation, as well as the well-known Schmidt model for the analytical description of pressure and volume throughout the cycle. A numerical simulation is then performed in MATLAB, where the work per cycle is calculated, p–V and T–s diagrams are generated, and the theoretical efficiency is evaluated for different operating temperatures and pressures. The simulation results show that increasing the temperature difference and average gas pressure significantly increases the mechanical output of the engine and the power output, while an efficient regenerator significantly improves the overall performance and brings the engine closer to Carnot efficiency. The study shows that the Stirling engine has significant potential for sustainable power generation systems, while the developed modeling and simulation framework provides a solid foundation for further experimental development and design optimization.*

Keywords*: STIRLING ENGINE, THERMODYNAMIC MODELING, MATLAB SIMULATION, MATLAB GUI.*

1. Introduction

The growing global demand for sustainable and efficient energy conversion technologies has renewed interest in external combustion systems, such as Stirling engines. First introduced in the 19th century and later formalized by Walker, Senft, Organ and other seminal authors [1–4], the Stirling engine operates in a closed regenerative thermodynamic cycle, capable of achieving efficiencies approaching the ideal Carnot limit. Its ability to utilize a wide range of heat sources, including fossil fuels, industrial waste heat, geothermal sources and solar radiation, makes the Stirling engine an attractive candidate for modern distributed energy applications, particularly in low-emission and high-reliability micro-generation systems [5,6].



Fig. 1 *Stirling Engine CAD Model [7].*

A distinctive feature of the Stirling cycle is its completely closed working fluid cycle, in which energy is transferred through expansion and compression processes separated in space by heat exchangers. Recent literature emphasizes the importance of regenerator design, dead volume minimization, and accurate thermodynamic modeling for predicting the behavior of the real cycle [8, 9]. Modern studies have further incorporated numerical simulation tools such as MATLAB [10] to evaluate the performance of the system under different conditions, enabling detailed analyses of p–V, T–s, and instantaneous pressure evolution [11]. Advances in computational modeling have also allowed researchers to incorporate non-ideal behaviors, including heat losses, pressure drops, regenerator inefficiencies, and, as highlighted in this study, the temperature-dependent (polynomial) variation of specific heat capacities, which provides a more realistic representation of the thermophysical properties of real gases over a wide temperature range.

Solar-powered, low-temperature differential Stirling engines have been of particular interest due to their simplicity, safety, and low cost of utilizing renewable thermal energy [12, 13]. Studies by Kongtragool et al. [12], and Shazly et al [9], demonstrate the feasibility of using solar radiation as the primary heat source, enabling micro-CHP and stand-alone power units for remote locations.

2. Methodology

The methodology of this study integrates classical thermodynamic theory with advanced numerical simulation techniques to develop a comprehensive and accurate model of the Stirling engine cycle. The engine is treated as a closed, regenerative thermodynamic system operating with an ideal working gas, following the fundamental approaches of Walker, Senft, Organ and Reader & Hooper [1–4]. Several standard engineering assumptions are adopted to simplify the modeling process without compromising physical accuracy. The working fluid is assumed to obey the ideal gas law throughout the cycle, and all processes are treated as internally reversible, with expansion and compression modeled as ideal isothermal transformations and heat transfer along isochores estimated using temperature-dependent thermodynamic properties. Kinetic and potential energy changes are neglected due to their negligible contribution to thermodynamic energy interactions, and the regenerator is modeled using an efficiency factor that considers real, non-ideal heat transfer. The heater, cooler, and regenerator are treated as separate control volumes to capture the spatial distribution of temperature and heat exchange mechanisms.

A central element of the methodology is the use of a temperature-dependent polynomial representation of specific heat capacities. To achieve high-fidelity modeling over a wide

temperature range, the NASA seven-term polynomial formulation is employed, following the procedures reported in Shazly et al. [7].

This approach allows accurate computation of Cp(T), Cv(T), enthalpy, and entropy as functions of temperature by integrating the polynomial expressions. In contrast to simplified constant-k models commonly found in classical analyses, this formulation provides a more realistic depiction of real-gas behavior and directly influences the accuracy of energy balances along the isochoric processes. The resulting thermodynamic representation yields more reliable estimates of work, heat transfer, and efficiency, particularly at elevated operating temperatures.

To determine the instantaneous pressure throughout the cycle, the Schmidt analytical model is adopted [6]. This model assumes sinusoidal piston–displacer kinematics and provides a closed-form expression for the pressure as a function of the engine's geometric characteristics, dead volumes, phase angle between piston and displacer, and heater and cooler temperatures. It allows the construction of continuous pressure–volume diagrams and captures dynamic variations that extend beyond the idealized Stirling cycle. The model's analytical nature ensures numerical stability and computational efficiency, making it suitable for iterative simulations and parametric studies.

All thermodynamic formulations are implemented in MATLAB, which serves as the main tool for numerical simulation [10]. The software calculates state properties such as temperature, pressure, enthalpy, and entropy for each process, and generates the corresponding p–V and T–s diagrams. Users specify initial conditions including the working gas mass, hot and cold side temperatures, volume ratio, and geometric parameters of the model. MATLAB then evaluates temperature-dependent specific heats, calculates heat interactions along isochores, determines the work produced by each isothermal process, and constructs the full pressure profile using the Schmidt model. Key performance indicators such as net cycle work, heat input, and thermal efficiency are obtained by integrating the pressure–volume curve and evaluating the energy balances for each transformation. The implementation also allows comparative analysis between models with constant and variable specific heats, enabling the assessment of the impact of real gas thermodynamic behavior on engine performance. Through this integrated methodology, combining thermodynamic fundamentals, polynomial-based property estimation, dynamic pressure modeling, MATLAB simulation, and prototype-oriented design, the study creates a powerful framework for accurately analyzing and improving the performance of Stirling engines intended for micro-scale power generation.

3. Results

The Stirling Engine MATLAB graphical interface provides an interactive environment for simulation, visualization, and thermodynamic analysis of ideal Stirling engine cycles, integrating mathematical modeling with modern digital concepts of Industry 4.0 for engineering education, research, and design optimization.

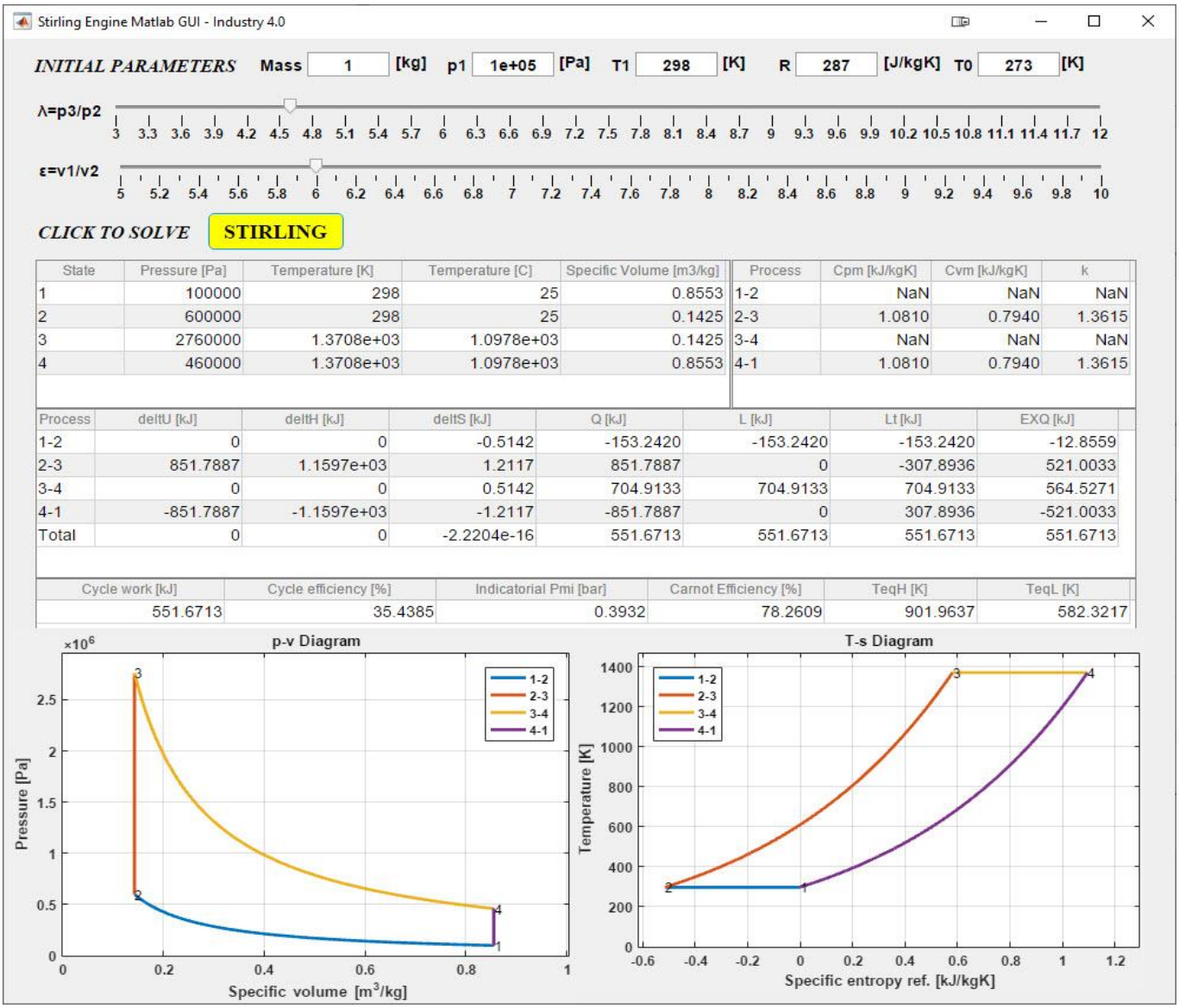
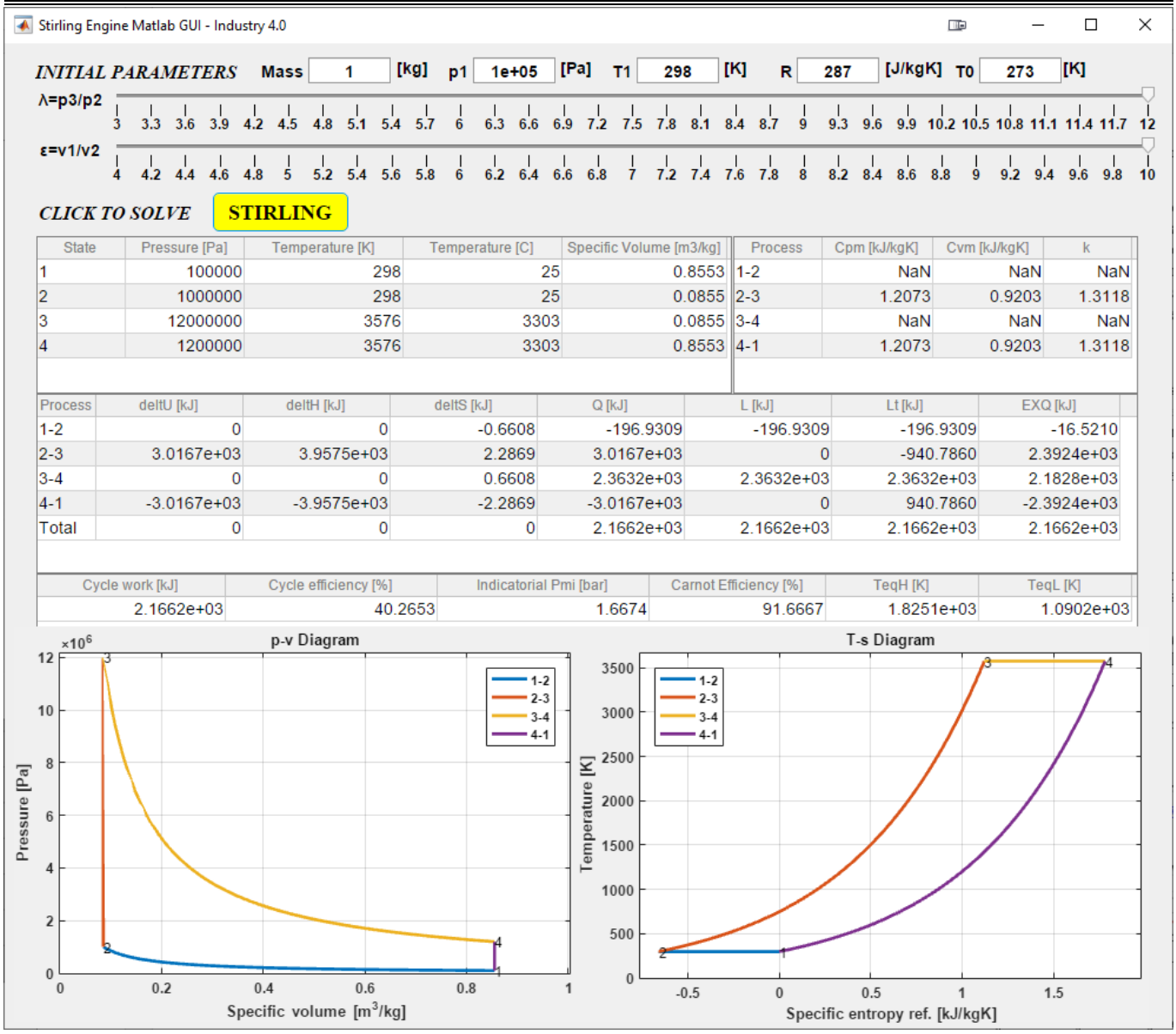


Fig. 2 *Thermodynamic analysis of ideal Stirling engine cycles.*



State	Pressure [Pa]	Temperature [K]	Temperature [C]	Specific Volume [m3/kg]
1	100000	298	25	0.8553
2	1000000	298	25	0.0855
3	12000000	3576	3303	0.0855
4	1200000	3576	3303	0.8553

Process	Cpm [kJ/kgK]	Cvm [kJ/kgK]	k
1-2	NaN	NaN	NaN
2-3	1.2073	0.9203	1.3118
3-4	NaN	NaN	NaN
4-1	1.2073	0.9203	1.3118

Process	deltU [kJ]	deltH [kJ]	deltS [kJ]	Q [kJ]	L [kJ]	Lt [kJ]	EXQ [kJ]
1-2	0	0	-0.6608	-196.9309	-196.9309	-196.9309	-16.5210
2-3	3.0167e+03	3.9575e+03	2.2869	3.0167e+03	0	-940.7860	2.3924e+03
3-4	0	0	0.6608	2.3632e+03	2.3632e+03	2.3632e+03	2.1828e+03
4-1	-3.0167e+03	-3.9575e+03	-2.2869	-3.0167e+03	0	940.7860	-2.3924e+03
Total	0	0	0	2.1662e+03	2.1662e+03	2.1662e+03	2.1662e+03

Cycle work [kJ]	Cycle efficiency [%]	Indicatorial Pmi [bar]	Carnot Efficiency [%]	TeqH [K]	TeqL [K]
2.1662e+03	40.2653	1.6674	91.6667	1.8251e+03	1.0902e+03

Fig. 3 *Thermodynamic analysis of ideal Stirling engine cycles (maximum volume ratio (ε) and pressure ratio (λ))*

The images below show an advanced version of the MATLAB graphical interface of the Stirling engine, displaying the results of multiple simulations of the Stirling cycle with different parameter values. The left graph illustrates the p–V diagram, each of which corresponds to a complete thermodynamic cycle for different combinations of volume ratio (ε) and pressure ratio (λ). The characteristic shape of the Stirling cycle loop is evident in all cases, with higher values of λ and ε producing wider loops and higher maximum pressures. The right graph presents the corresponding T–s diagrams, where the isothermal and isochoric segments of the cycle become more pronounced as the temperature levels increase. The curves demonstrate the impact of changing the parameters on entropy generation and thermal load.

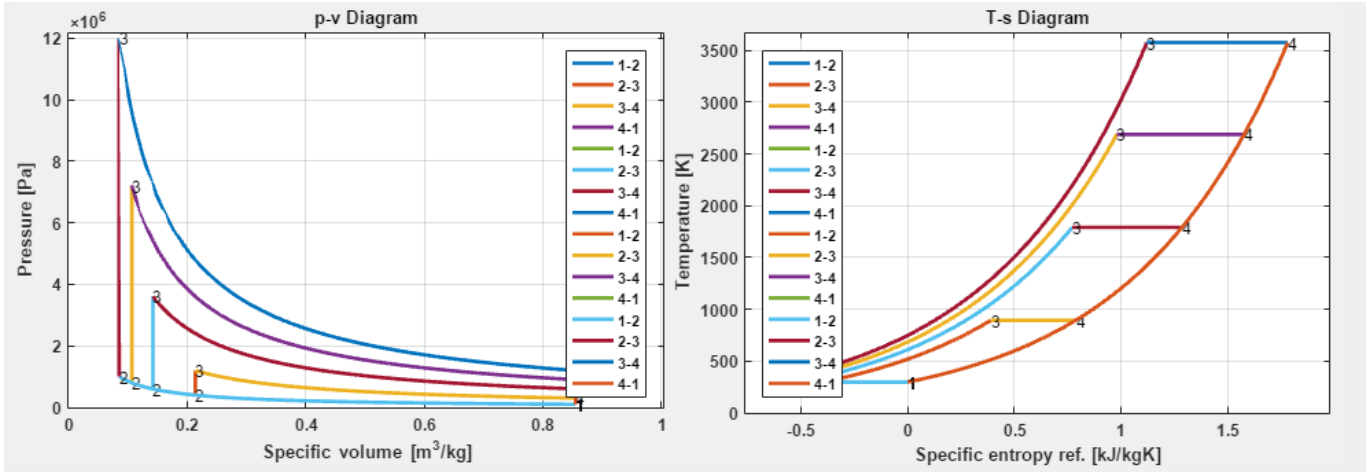


Fig. 4 *Stirling Engine p–V and T–s diagrams of multiple Stirling cycle simulations with varying parameter values.*

The graphical user interface (GUI) was fully coded in MATLAB App Designer [10], providing a clear and intuitive layout where users can enter all relevant thermodynamic parameters, run numerical simulations, and visualize p–V and T–s diagrams in real time. The program architecture is based on fundamental thermodynamic principles [1-6], including the ideal gas law and energy balance equations for each process of the Stirling cycle: isothermal expansion (1–2), isochoric regeneration (2–3), isothermal compression (3–4), and isochoric heat rejection (4–1).

In the control panel, users can specify initial parameters such as the mass of the working gas, the initial pressure and temperature, the pressure and volume ratios (λ and ε), and the universal gas constant (R). Once these parameters are entered, the user starts the calculation by clicking "STIRLING", which activates the computer solver built into the GUI.

The central table dynamically displays state properties (pressure, temperature, specific volume, enthalpy, entropy, and internal energy) in all four thermodynamic states, along with process-related variables such as heat transfer (Q), work (L), enthalpy change (Δh), internal energy change (Δu), and entropy change (Δs). These data are calculated numerically using logarithmic and exponential relationships for each process, ensuring physical consistency and high computational accuracy.

The interface automatically generates two main graphical outputs, the p–V diagram, illustrating the cyclic behavior of pressure versus specific volume, clearly showing the closed thermodynamic loop. The closed area corresponds to the net work output per cycle, and the T–s diagram, showing the evolution of temperature in relation to specific entropy, highlighting the reversible nature of the ideal cycle, and allowing comparison with the reference Carnot efficiency.

The bottom section of the GUI summarizes the cycle performance metrics, including, Cycle Work [kJ], Thermal Efficiency [%], Mean Indicated Pressure (Pmi) [bar], Equivalent Carnot Efficiency [%], Average Effective Temperatures of the Heater (TeqH) and Cooler (TeqL).

The Stirling Engine's MATLAB graphical user interface can be used in a wide range of academic and research applications, serving as a powerful tool for both teaching and advanced analysis. It is particularly well-suited for academic teaching and demonstration of closed-loop thermodynamic processes, allowing students to visualize and understand the energy transformations within the Stirling cycle.

Beyond its analytical capabilities, the software has strong educational integration potential, functioning as a didactic platform for thermodynamics, energy systems, and sustainable engineering curricula, fully aligned with the principles of the digital transformation of Industry 4.0 laboratories.

4. Conclusions

This original MATLAB-based simulation environment demonstrates a successful fusion of theoretical modeling, computer automation, and graphical representation, embodying the principles of digital transformation in engineering education. Through its versatility and precision, the MATLAB Stirling Engine GUI stands as an innovative tool for advancing the understanding and design of high-efficiency thermodynamic systems.

The Stirling engine represents a thermodynamic system characterized by high theoretical efficiency, capable of approaching the Carnot limit due to its operation based on the temperature difference between the heat source and the heat sink. Its externally heated configuration allows flexible use of various thermal energy sources, including renewable and waste heat, while maintaining low emissions and high reliability.

The simplified mathematical modeling approach, founded on the ideal gas law and the division of the working space into hot and cold chambers, provides a clear insight into the pressure and volume variations throughout the thermodynamic cycle. The resulting p–V diagram displays a closed loop whose enclosed area represents the net work output, confirming the energy-conversion capability of the engine.

Numerical simulations performed in MATLAB enable detailed investigation of how key operational parameters, such as hot and cold temperatures, mean working pressure, and compression ratio affect the indicated work and overall efficiency. These simulations constitute an essential tool for parametric optimization and facilitate direct comparisons with other thermodynamic cycles under similar boundary conditions.

To improve accessibility and usability in academic environments, the final version of this tool will also be compiled into a standalone .exe application for Windows. This executable version will allow students and academic staff to use the software without the need for a MATLAB license, making it fully distributable in teaching labs, classrooms, training sessions, and distance learning platforms. Creating a dedicated executable file ensures faster performance, higher stability, and seamless integration with the Windows operating system, transforming this GUI into a practical and widely accessible tool for education and research.

5. References

1. Walker, G. "*Stirling Engines"*. Oxford: Clarendon Press, (1980).
2. Senft, J. R. "*An Introduction to Stirling Engines"*. Moriya Press. (1993).
3. Organ, A. J. "*Thermodynamics and Gas Dynamics of the Stirling Cycle Machine"*. Cambridge University Press. (1992).
4. Reader, G. T., & Hooper, C. "*Stirling Engines"*. Longman Group Limited. (1983).
5. Çengel, Y. A., & Boles, M. A. "*Thermodynamics: An Engineering Approach. 8th ed"*. New York: McGraw-Hill; (2015)
6. Schmidt, "*Schmidt Analysis for Stirling engines*." (1972).
7. *https://www.3dcadbrowser.com/3d-model/stirling-engine-38917*
8. Ana C. Ferreira, Ricardo F. Oliveira, Manuel L. Nunes, Luís B. Martins, and Senhorinha F. Teixeira *"Modelling and Cost Estimation of Stirling Engine for CHP Applications", (2014).*
9. J.H. Shazly, A.Z. Hafez, E.T. El Shenawy, M.B. Eteiba. *Simulation, design and thermal analysis of a solar Stirling engine using MATLAB.* Energy Conversion and Management. (2014).
10. MATLAB Documentation. "*MATLAB & Simulink for Numerical Simulation of Thermodynamic Cycles"*. MathWorks; (2025).
11. Gjeta, A., Alcani, M., Dorri, A., "*The Influence of Thermodynamic Parameters on Internal Combustion Engines and the Graphical Presentation of Cycles Diagrams Using Matlab"*. Lecture Notes on Multidisciplinary Industrial Engineering. Springer, Cham. https://doi.org/10.1007/978-3-031-48933-4_28, (2024).
12. Kongtragool, B., & Wongwises, S. "*A review of solar-powered Stirling engines and low-temperature differential Stirling engines"*. Renewable and Sustainable Energy Reviews, 7(2): 131–154. (2003).
13. F. Formosa and G. Despesse, "*Analytical model for Stirling cycle machine design"* Energy Convers. Manag., vol. 51, no. 10, pp. 1855–1863, Oct. (2010).

Research on deformations of a flexible screw sectional working body

Volodymyr Bulgakov, Oleksandra Trokhaniak, Stanislav Kovalchuk, Olha Dubrovina
National University of Life and Environmental Sciences of Ukraine, Kyiv, Ukraine
E-mail: vbulgakov@meta.ua

Abstract. *The article presents the construction of a flexible sectional screw working body, the use of which allows to improve the performance of flexible screw conveyors with low material consumption of the working body, which reduces energy costs for the transportation process. Based on the results of static experimental studies, the nature of the change in the dependence of torque on the angle of twist of individual sections has been established.*
KEYWORDS: *TRANSPORTATION, DAMAGED SOIL, SCREW WORKING BODY, CRATER.*

Introduction

The biggest impact on farmland and soil cover comes from enemy air and artillery attacks, which account for about 80% of the damage. As a result of rocket and artillery shelling, fields are covered with craters from explosions of shells, mines, and rockets. These craters vary in diameter and depth [1].

Therefore, transforming contaminated land into usable areas and preserving the fertility of agricultural soils is a pressing issue for ensuring Ukraine's food security.

To restore areas damaged by explosions, it is necessary to remove or clean the topsoil, since, in addition to chemical contamination with heavy metals, the fertile soil layer is also burned out. To carry out technical reclamation of land damaged by bombing, a method has been proposed that involves first cleaning the craters of damaged and contaminated soil with heavy metals and other hazardous substances. A flexible screw conveyor with a sectional screw working body can be used to dispose of the removed contaminated soil layer, which will make it possible to overload it into a truck body.

Screw conveyors are most widely used for transporting various types of bulk agricultural materials, including grain, granulated seed materials, clay, sand, loose soil, mixed feed, mineral fertilizer granules, etc.

After all, the basis for the comprehensive mechanization of loading and unloading operations, which increase labor productivity and production efficiency, is the technical means of continuous transportation of agricultural bulk materials. The transportation of grain and seed materials along straight, curved, and combined routes using flexible screw working bodies enclosed in elastic casings ensures high productivity and mobility during the implementation of various technological processes and, accordingly, expands their technological capabilities and ensures a reduction in energy costs.

The main disadvantage of rigid screw conveyors is the limited mobility of technological lines. In addition, the placement of the screw shaft in supports and a rigid guide pipe leads to increased material consumption in the construction of such conveyors [2, 3].

Based on the analysis of the literature, it can be concluded that the least resource-intensive technology for moving bulk agricultural materials along curved routes is the use of flexible screw conveyors, which are made on the basis of separate screw sections that are hinged together [4, 5]. In works [6-8], the design, kinematic, and technological parameters of screw working bodies are justified from the point of view of their functional purpose.

To eliminate these shortcomings, active research has recently been conducted to find optimal designs for flexible screw conveyors with expanded functional and operational characteristics [9, 10]. In such conveyors, the flexible screw working body is freely (without supports) located in an elastic casing and moves the material to the unloading zone with its inner surface, which is their main advantage.

Rotating at a frequency of over 550 rpm, the flexible screw spiral actually distributes the bulk material evenly around the periphery of the conveyor casing, which causes it to self-center and ensures the movement of the product to the unloading zone [11, 12].

Based on the results of the conducted research, the structural, kinematic, and technological parameters of the working parts of a flexible screw conveyor have been substantiated in terms of their functional purpose [13, 14]. At the same time, a number of issues regarding the operational and resource indicators of such working parts remain unresolved. This indicates that improving the efficiency of flexible screw conveyors is an important and urgent task for agricultural production.

Therefore, it is urgent to develop new designs and substantiate the parameters of flexible screw working bodies that will improve the functional and operational performance of conveyors.

Results and discussion

A flexible screw conveyor with a sectional screw working body can be used to dispose of the removed contaminated soil layer, which will allow it to be transferred to a truck body.

Fig. 1 shows a structural diagram of such a flexible screw sectional working body for transporting damaged soil. This working body consists of separate sections of the same diameter and length, which are made in the form of welded structures containing rods 1, to which a cylindrical sleeve 2 is rigidly attached at one end, made with a system of axial parallel grooves evenly spaced around the circumference, which interact with balls 3. On the other side, balls 3 interact with spherical holes in the body 4, which allows for axial and angular rotation of the spherical pin 5. In addition, the top of the cylindrical sleeve 2 is in rigid interaction with the spherical body 4, the inner surface of which interacts with the outer surfaces of the balls 3. At the other end of the welded cylindrical section, a connecting sleeve 6 is rigidly installed in the inner hole, perpendicular to the axis, which interacts with the corresponding end of the spherical pin 5 of the adjacent section and rigidly fixes it with a bolt connection 7.

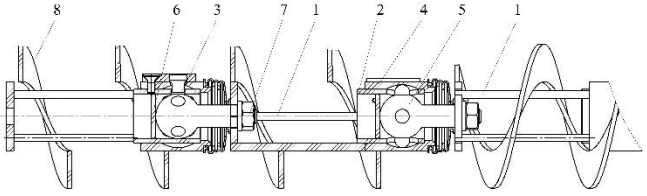
A screw section 8 is rigidly welded to the outer diameter of the cylindrical section.

The screw working body operates as follows. When the spiral section 8 rotates, the rotational motion is transmitted through balls 3 to the spherical pin 5 and adjacent sections of the screw working body.

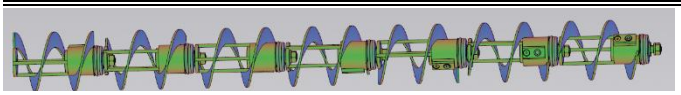
In order to establish the adequacy of the theoretical study, static experimental studies of the sectional working body were carried out, which made it possible to determine the torque depending on the relative angular displacement of the end surfaces.

The studies were conducted using the following methodology. To conduct the experiments, the section of the hinged sectional working body was installed in the clamps of the KM-50-1 test machine.

The load on the section was applied by rotating the lower gripper with an electric motor through a transmission system. The torque value was determined using a circular scale, while the relative displacement of the end surfaces of the working body was recorded using an angular scale. The machine is also equipped with a recording device, which is used to plot the curve of torque dependence on the angle of rotation of the lower gripper.



a



b

Figure 1. *Design diagram (a) and general view (b) of a flexible screw sectional working body*

Three variants of experimental samples were manufactured: two single screw sections with two and four longitudinal rods, respectively, as well as a part of the working body made of two sections. Photographs of the manufactured variants of experimental samples are shown in Fig. 2.



a b

Figure 2. *General view of screw working body section samples: a) screw section with two longitudinal rods; b) screw section with four longitudinal rods*

The manufactured sections of the screw working body had the following design parameters: outer diameter of the spiral D = 96 mm; width of the spiral B = 25 mm; thickness of the spiral t = 4 mm; length of the section L = 130 mm; diameter of the longitudinal rod d = 5 mm.

The general view of the KM-50-1 torsion machine with experimental samples of working body sections is shown in Fig. 3.

During the study, discrete loading of the screw section was performed, where the torque value and the corresponding angle of twisting of the end surfaces of the sections were simultaneously recorded. Experimental studies were carried out until residual deformations appeared on the section elements.

The studies for different variants of sections and their connections were carried out three times.

Based on the results of the experimental studies, graphical dependencies of the torque on the section and connected sections on the angle of twisting of the end elements were constructed, which are shown in Fig. 4.

Their analysis shows that for individual sections without hinged connections (curves 1 and 2), the functional dependence has a clearly linear character. Moreover, for the above-mentioned design parameters of screw sections, a further increase in torque led to the appearance of residual deformations, which is unacceptable.



Figure 3. *General view of the KM-50-1 twisting machine with experimental samples of working body sections*

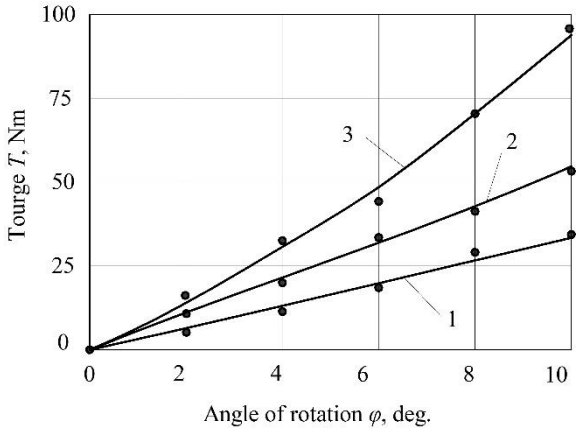


Figure 4*. Graphical dependencies of torque T variation on the section from the angle of twisting of the end surfaces:*
1 – screw section with four longitudinal rods;
2 – screw section with two longitudinal rods;
3 – two sections with two longitudinal rods connected to each other by an elastic element

The curvilinear nature $T = f(\varphi)$ within the range of 40...60 Nm for two sections connected to each other is explained by the fact that the appearance of additional hinge links causes a more intense increase in the angle φ with an increase T due to manufacturing inaccuracies and the occurrence of local gaps. With a further increase in the value T > 60 Nm the curve $T = f(\varphi)$ transitions into a clearly expressed linear dependence.

It has also been established that for assembled sections, an increase in torque above 100 Nm leads to the appearance of residual deformations on the sectional elements.

Conclusions

The article presents the design of a flexible sectional screw working body, the use of which allows to improve the performance of flexible screw conveyors with low material consumption of the working body, which reduces energy costs for the transportation process.

Based on the results of static experimental studies, it has been established that the dependence of torque on the twist angle ($T = f(\varphi)$ of individual sections has a clearly pronounced linear character. The curvilinear character $T = f(\varphi)$ within the range of 40...60 Nm for two assembled sections is explained by the occurrence of local gaps. With a further increase in the value of T > 60 Nm, the curve has a linear dependence. It has been established that an increase in torque above 100 Nm leads to the appearance of residual deformations on the sectional elements.

References

1. Balyuk S.A., Kucher A.V., Solokha M.O., Solovei V.B., Smirnov K.B., Momot G.F., Levin A.Ya. (2022). The influence of armed aggression and military actions on the current state of the soil cover, damage and loss assessment, restoration measures. Kharkiv: FOP Brovin O.V., 2022, 102 p.

2. Bulgakov V., Trokhaniak O., Klendii M. et al. Research on the Impact of the Operating Modes and Main Design Parameters on the Efficiency of the Machine for Preparing and Packing Slaked Lime. INMATEH: Agricultural Engineering. 2022. 67(2). P. 323–330. doi: 10.35633/inmateh-67-33.

3. Hevko R.B., Klendiy M.B., Klendiy O.M. Investigation of a transfer branch of a flexible screw conveyor. INMATEH – Agricultural engineering. 2016. V. 48. № 1. P. 29–34.

4. Lech M. Mass flow rate measurement in vertical pneumatic conveying of solid. Powder Technology. 2001. V. 114. Is. 1–3. P. 55–58.

5. Hevko R.B., Rohatynskyi R.M., Rozum R.I. et al. Increasing the technological level of loading and reloading processes of

materials in screw conveyors: monograph. Ternopil: Osadtsa Yu.V., 2018. 180 p.

6. Bulgakov V., Olt J., Ivanovs S. et al. Research of a contact stresses in swivel elements of flexible shaft in screw conveyor for transportation of agricultural materials. Estonian Academic Agricultural Society. Agraarteadus. 2022. 33(1). P. 67–73. doi:10.15159/jas.22.12

7. Pylypaka S.F., Klendii M.B., Klendii O.M. Particle motion over the surface of a rotary vertical axis helicoid. (2017) INMATEH - Agricultural Engineering, 51 (1), pp. 15–28.

8. Hevko R.B., Rozum R.I., Klendiy O.M. Development of design and investigation of operation processes of loading pipes of screw conveyors, INMATEH: Agricultural engineering. 2016. V. 50. №. 3. P. 89–94.

9. Hevko R., Rohatynskyi R., Hevko M. et al. Investigation of sectional operating elements for conveying agricultural materials. Research in Agricultural Engineering. 2020. 66(1), 18–26. The website of the journal: https://www.agriculturejournals.cz/publicFiles/25_2019-RAE.pdf

10. Hevko R., Vitrovyi A., Klendii O., Liubezna I. Design engineering and substantiation of the parameters of sectional tools of flexible screw conveyors. Bulletin of the Transilvania University of Brasov. 2017. V. 10 (59). pp. 39–46.

11. Bulgakov V., Olt J., Ivanovs S. et al. Research of a contact stresses in swivel elements of flexible shaft in screw conveyor for transportation of agricultural materials. Agraarteadus. 2022. V. 33. № 1. P. 67–73. doi: 10.15159/jas.22.12

12. Trokhaniak O.M., Hevko R.B., Lyashuk O.L., Dovbush T.A., Pohrishchuk B.V., Dobizha N.V. Research of the of bulk material movement process in the inactive zone between screw sections. (2020) INMATEH – gricultural Engineering, 60 (1), pp. 261–268.

13. Hevko R.B., Zalutskyi S.Z., Hladyo Y.B., Tkachenko I.G., Lyashuk O.L., Pavlova O.M., Pohrishchuk B.V., Trokhaniak O.M., Dobizha N.V. Determination of interaction parameters and grain material flow motion on screw conveyor elastic section surface. (2019) INMATEH – Agricultural Engineering, 57 (1), pp. 123–134.

14. Bulgakov V., Trokhaniak O., Adamchuk V., Chernovol M., Korenko M., Dukulis I., Ivanovs S. A Study of Dynamic Loads of a Flexible Sectional Screw Conveyor. (2022) Acta Technologica Agriculturae, 25 (3), pp. 131–136.

Investigation of the parameters of a curved channel of the confuser type

Viktor Trokhaniak

National University of Life and Environmental Sciences of Ukraine, Kyiv, Ukraine
E-mail: vbulgakov@meta.ua

Abstract. *Parametric optimization of a curved channel was made with changing the geometric shape under pre-set conditions when liquid or gas flows through it. Mathematical modelling of hydrodynamic processes was performed in curved channels of the confuser type. As a result of numerical modelling of the hydrodynamic processes, using the ANSYS Fluent CAD software product, the distributions of velocities and pressures in the confuser channel were obtained. The optimal curved channel profile was selected. based on the conditions of minimal pressure losses in the channel. The obtained results may be used in the design of the heat exchange and aerodynamic equipment.*

KEYWORDS: *PARAMETRIC OPTIMIZATION, CURVED CHANNELS, CONFUSER, PRESSURE, VELOCITY), LAMINAR FLOW.*

Introduction

When designing devices with hydrodynamic flows, an important feature of the flow channels is the pressure loss in these channels when the liquid or gas is flowing. Such channels are found, for example, in the wind generators, turbines, heat exchangers, etc. Therefore it is necessary to select a channel geometry that will minimize these losses. An optimal geometry of the channel is determined as a result of solving an optimization problem by changing the geometric shape of the channel, with constant parameters of the liquid or gas flowing through it.

Wang et al. [1] presented multi-objective optimization algorithms to optimize the compactness, pressure drop, and thermal performance of AFF PCHE under different inlet velocity conditions. Said et al. [2] optimized C-shaped PCHEs by combining multi-objective genetic algorithm (MOGA), machine learning, and CFD modelling. Zeng et al. [3] presented an improved PSO-BP neural network, combined with NSGA-II algorithm, to design AFF PCHE. Jiang et al. [4] selected four parameters to optimize the AFF PCHE by integrating machine learning, CFD modelling and optimization algorithms.

In recent years, Bezier curves have attracted considerable attention due to their effectiveness as a method for parametrizing shapes in aerodynamic studies [5], [6], [7]. However, the studies have not yet been used to optimize the thermal-hydraulic characteristics of the AFF PCHE. The Bezier curve is defined by a set of control points Pk with m+1 parameters [8].

As a continuation of the study, the authors [9, 10] conducted an experimental research of a new design of the wind flow concentrator, using an aerodynamic subsonic wind tunnel. As a result, it was found that in the area of the wind generator blades, the speed of the air masses increases 4 times, compared to the speed of air at the entrance to the wind flow concentrator. An assessment was made of the use of a wind flow concentrator to improve the efficiency of the vertical axis wind turbines.

When optimizing a curved channel, the best solution of the problem is to select such parameters of the curved channel that meet the specified requirements for the channel geometry, as well as the conditions and limitations for the hydrodynamic flow in this channel. In a mathematical optimization problem the solution is formulated as a search for the extremum (maximum or minimum) of a given objective function [11]. The objective function is known a priori and is determined by an analytical dependence on one or more independent arguments (parameters).

If a function $F\{X\}$ is defined on a set X from an n-dimensional Euclidean space Rn that has extreme values, then the optimization problem consists of finding the extrema of this objective function.

$$\text{Extr } F(X), \text{ where } X \epsilon Rn. \quad (1)$$

In the future, we will consider only the minimization problem of a function for which we can also reduce the problem of finding the maximum of a function. we will consider only the problem of minimizing a function, for which we can also reduce the problem of finding a maximum of the function.

$$\min F(X), \text{ where } X \epsilon Rn. \quad (2)$$

The solution to the optimization problem consists of finding the global minimum X*, where the objective function has the smallest value over the entire feasible region

$$F(X^*) \leq F(X), \forall X \epsilon Rn. \quad (3)$$

Based on the analysis of literary sources, it can be concluded that the issues of optimization of curvilinear channels, which are used in various power plants, have not been sufficiently studied. Therefore it is relevant to solve the optimization problems for such channels that make it possible to reduce the aerodynamic flow resistance and improve the characteristics of the energy devices.

Результати та обговорення

In order to analyse the influence of different geometric dimensions and improve the performance of the curved channel, structural variables, corresponding to diverse geometric dimensions of the channel, were defined and varied within certain limits. In this parametric model of a curvilinear channel a layout scheme has been developed, the analysis of which determines all channel control parameters [12, 13]. These are the main dimensions that control all the other dimensions of the 2D channel model (Fig. 1). The main parameter is the radius of the arc of the channel sidewalls R1. For this parameter the corresponding variables considered are the main variables of the 2D model parameters. The dimensions of radius R2 (inlet to the channel) and R3 (outlet from the channel) remain unchanged.

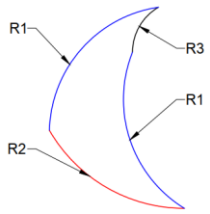


Figure 1. *External appearance of a curved channel*

To solve the problem of parametric optimization of a curved channel, using static and dynamic parameters, the radius of the arc of the side wall of the channel was used as a variable main parameter. It varied over a wide range (from 110 mm to 250 mm) with a step of 20 mm. The area was monitored with the highest values of velocity and pressure at the channel outlet (with radius R3).

During the optimization process, based on the main geometric dimensions of the channel, the values of the optimization parameters were selected in such a way that, when changing the channel dimensions, they would allow for minimal hydraulic losses for maximum flow velocity at the exit from the channel.

For the investigation there was used commercial software ANSYS Fluent to solve the equations of the flow in the channel. Mathematical modelling of the processes of the air mass transfer in a curved confuser-type channel applying the Navier-Stokes equation in a two-dimensional formulation in the laminar flow mode, which is typical for the movement of the air flows in channels of this type:

$$\left.\begin{aligned}\rho\left(\frac{\partial u}{\partial t}+u\frac{\partial u}{\partial x}+v\frac{\partial u}{\partial y}\right)&=-\frac{\partial p}{\partial x}+\mu\left(\frac{\partial^2 u}{\partial x^2}+\frac{\partial^2 u}{\partial y^2}\right),\\ \rho\left(\frac{\partial v}{\partial t}+u\frac{\partial v}{\partial x}+v\frac{\partial v}{\partial y}\right)&=-\frac{\partial p}{\partial y}+\mu\left(\frac{\partial^2 v}{\partial x^2}+\frac{\partial^2 v}{\partial y^2}\right),\end{aligned}\right\} \quad (4)$$

$$\frac{\partial u}{\partial x}+\frac{\partial v}{\partial y}=0.$$

The following boundary conditions are set for the walls of the channel and at its inlet and outlet:

$$\begin{aligned}&u(t=0)=v(t=0)=0;\\ &npu \quad x=x_{i,wall},\ y=y_{i,wall};\ i=1,2;\\ &u=v=0,\ \frac{\partial u_{i,wall}}{\partial \bar{n}}=\frac{dv_{i,wall}}{\partial \bar{n}}=0,\\ &npu \quad x=x_{in};\ y=y_{in};\quad u_{in}=v_{in}=W_0;\\ &npu \quad x=x_{out};\ y=y_{out};\quad \frac{\partial u_{out}}{\partial x}=\frac{\partial v_{out}}{\partial y}=0.\end{aligned} \quad (5)$$

The following notations are adopted for this model: x, y – Cartesian coordinates; t – time; u, v – velocity components; ρ – density of the liquid or gas; $\bar{n}$– normal vector on the channel wall; indices i=1,2 and *wall* denote the walls of the channel; *in*, *out* – the inlet and outlet of the channel; W_0 – air velocity at the inlet of the channel.

Numerical modelling of the hydrodynamic processes in a curved confuser-type channel was performed using the ANSYS Fluent software product. A computational grid has been constructed in the channel, which has refinement near the walls.

There was performed a numerical calculation of the dynamic characteristics of the flow in the channel to be investigated.

As a result of numerous calculations, the pressure distribution in the channel was obtained. There is a pressure drop at the outlet of the channel. In quantitative terms, however, the magnitude of this drop is insignificant, which is due to the curvature of the surface for the air flow in the channel.

As one can see from the obtained distributions, the maximum values of speed are observed at the end of the channel. At the surface of one of the walls of the channel there is a stagnant zone in which the air moves at a low speed, changing the direction of its movement from the inlet to the outlet.

The optimization parameter is selected as the objective function, which is the ratio $K = P/V$, characterizing the change in the loss of pressure with a change in the flow velocity, where P and V are the average values of pressure and velocity at the outlet of the channel. The value of the radius of the curved wall $R1$ changed at constant values of other geometric characteristics of the channel.

The numerical calculation data obtained are presented in graphically represented in Fig. 2.

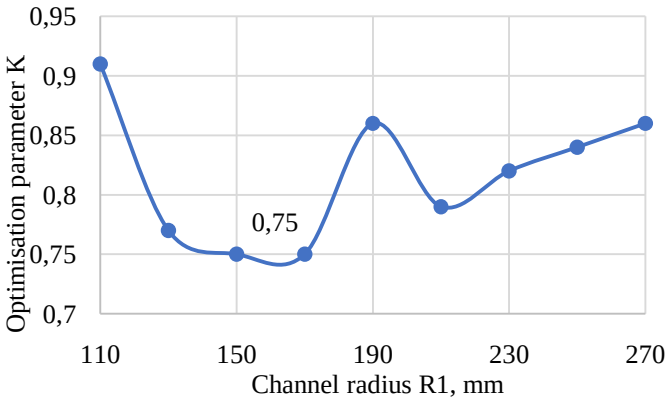


Figure 2. *Change in pressure and exit velocity from the channel with various values of the side wall radius*

As a result of the conducted research, it can be concluded that, with other output parameters remaining constant, the optimal value of the channel curvature radius is R1 = 150 mm.

The obtained data can be useful when developing equipment for various purposes – the wind generators, turbines, heat exchangers and other energy devices.

Conclusions

Two-dimensional parametric optimization was performed of a curved channel with the pre-set geometric dimensions. The influence of various geometric parameters upon the change in the pressure field and channel velocity is analysed in order to improve the aerodynamic characteristics of the curved channel. The conducted calculations of parametric optimization show that, with a radius of curvature of the side walls of the channel of 150 mm, the optimal values of parameter K are determined, which characterizes the smallest values of the pressure drop when changing the flow velocity in the channel.

Numerical modelling of the hydrodynamic processes in a channel with curved walls was carried out using the ANSYS Fluent software package. Local distributions of the velocity and pressure fields in a curved channel are obtained. It is shown that the use of curved channels reduces the size of stagnant zones, reduces pressure losses, which improves the aerodynamic and energy properties of the channel of the type under consideration.

The obtained data about the optimal geometry of the curved channels of the confusal type can be used in the development of energy devices for various purposes – the wind generators, turbines, heat exchangers and other elements of energy equipment.

References

1 Wang W., Li B., Tan Y., Li B., Shuai Y. Multi-objective optimal design of NACA airfoil fin PCHE recuperator for micro-gas turbine systems. Appl. Therm. Eng., Vol. 204 (2022), Article 117864

2 Saeed M., Berrouk A.S., Al Wahedi Y.F., Singh M.P., Dagga I.A., Afgan I. Performance enhancement of a C-shaped printed circuit heat exchanger in supercritical CO2 Brayton cycle: A machine learning-based optimization study. Case Stud. Therm. Eng., Vol. 38 (2022), Article 102276

3 Wang J., Zeng L., Yang K. Multi-objective optimization of printed circuit heat exchanger with airfoil fins based on the improved PSO-BP neural network and the NSGA-II algorithm. Nucl. Eng. Technol., Vol. 55 (2023), pp. 2125-2138

4 Jiang T., Li M.J., Yang J.Q. Research on optimization of structural parameters for airfoil fin PCHE based on machine learning. Appl. Therm. Eng., Vol. 229 (2023), Article 120498

5 Wang J., Wang C., Zhou B., Zeng L., Yang K. Airfoil shape and angle of attack optimization based on Bézier curve and multi-island genetic algorithm. J, Fluids Eng., Vol. 144 (2022), Article 051203

6 M.G. Lauer, P.J. Ansell. A parametrization framework for multi-element airfoil systems using Bézier curves. AIAA aviation 2022 forum (2022), p. 3525

7 Wei X., Wang X., Chen S. Research on parameterization and optimization procedure of low-Reynolds-number airfoils based on genetic algorithm and Bezier curve. Adv. Eng. Softw., Vol. 149 (2020), Article 102864

8 Keramati H., Hamdullahpur F., Barzegari M.. Deep reinforcement learning for heat exchanger shape optimization. Int. J. Heat Mass Transf., Vol. 194 (2022), Article 123112

9 Gorobets V.G., Trokhaniak V.I., Masiuk M.Yu., Spodyniuk N.A., Blesnyuk O.V., Marchishina Ye.I. CFD modeling of aerodynamic flow in a wind turbine with vertical rotational axis and wind flow concentrator. INMATEH-Agricultural Engineering. Vol. 64, no. 2, (2021), pp. 159-166.

10 Gorobets V.G., Trokhaniak V.I., Masiuk M.Yu., Spodyniuk N.A., Sheremetynska O.V., Shelimanova O.V. Experimental study of aerodynamic characteristics and evaluation of wind flow concentrator efficiency. INMATEH - Agricultural Engineering, Vol. 66, no. 1, (2022), pp. 257-266.

11 Attetkov A.V., Galkin S.V., Zarubin V.S. Optimization methods. Publishing house of Bauman Moscow State Technical University, 2001.

12 Antar E., Elkhoury M. Parametric sizing optimization process of a casing for a Savonius Vertical Axis Wind Turbine. Renewable Energy. Vol. 136, (2019), p. 127-138 https://doi.org/10.1016/j.renene.2018.12.092

13 orobets V., Aboltins A., Rucins A., Tkachenko M., Masiuk M., Trokhaniak V., Zhurylo D., Kuvachov V., Balian A. Parametric Optimization of a Curvilinear Confuser-Type Chanel (2025) Engineering for Rural Development, 24, pp. 615 - 621

Tribological Analysis of Plasma Spray Thermal Deposition on the Active Area of Harrow Discs

Corneliu Munteanu[1], Iurie Melnic[2*], Bogdan Istrate[1], Marcelin Benchea[1], Constantin Zîrnescu[2], Vladimir Badiul[2]
[1] "Gheorghe Asachi" Technical University of Iasi, 700050 Iasi, Romania
[2] Technical University of Moldova, 168, Ștefan cel Mare Blvd., Chișinău, Republic of Moldova
[*] iurie.melnic@im.utm.md

Abstract: *The results of tribological tests of the active area of harrow disks with coatings obtained by the plasma spay thermal method are presented. This study is based on scanning electron microscopy of coated harrow disc samples undergoing standard tribological tests that focuses on the mechanical properties of coatings using tribological methodology. Tribological studies were conducted to determine the following main parameters of the harrow disc material such as: adhesion to the substrate, coefficient of friction, Young's modulus, stiffness and hardness of coated samples and the base material. As the result, improving the mechanical and chemical properties of materials used to manufacture the working bodies of coated harrow discs allows for increased resistance to abrasive wear in modern agricultural machinery.*
KEY WORDS: *TRIBOLOGICAL ANALYSIS, PLASMA SPAY THERMAL METHOD, HARROW, COATED DISC, ACTIVE AREA.*

Introduction

The quality of manufactured tillage agricultural machinery does not allow for prevention severe wear of their working bodies. Increasing the durability of tillage equipment parts, such as harrow discs, is one of the main areas in the design and production of agricultural machinery, the use of which increases productivity, reduces costs and ensures the best results in farming.

Since harrow discs are also subject to severe abrasive wear as a result of soil cultivation, analysis of plasma-thermal spraying on the active part of harrow discs allows to evaluate the resistance to abrasion and corrosion.

A number of scientists has shown that all tillage machines wear out faster as the amount of sand particles in the soil increases, requiring improved mechanical properties of the working surfaces of the working parts [1, 2]. This suggests a relationship between the wear of the active area of the working bodies of the machine and the size of the sand particles and, as a consequence, the optimization of their mechanical properties to increase the wear resistance of the discs is crucial for extending the service life of the active area of the harrow discs [1, 2, 3].

During the soil tillage operation, the harrow disc blades are also subject to significant wear due to abrasive soil particles: sand, small stones and other hard materials accidentally found in the soil. Therefore, the active area of the working elements of these machines must have significant impact resistance [1, 2, 4, 5]. This means using effective methods to improve the required parameters of the active surface of the harrow discs, and subsequently conducting tests of disc harrows in accordance with current standards for testing agricultural machinery.

Plasma spray thermal deposition is one of the effective methods for improving the main parameters of the harrow disc material, considered an advanced method capable of achieving high-quality surface layers [2, 3]. It should be noted that the use of this method is usually limited to very thin coatings - up to 100 μm.

Prerequisites and means for solving the problem

Severe wear conditions require coatings that offer high hardness and durability, such as the often used tungsten carbide (WC) coatings, which consist of WC particles as a hard and resistant phase for wear protection. Once embedded in a metal matrix, the tungsten carbide particles act as a plastic binder, effectively bonding and supporting the carbide grains under severe operating conditions [6].

Carbide degradation, particle ejection, and subsurface crack formation play a significant role in the wear behavior of deposits. The study of erosive and abrasive wear of WC12Co and WC10Co4Cr coatings deposited by the High-Velocity Oxygen Fuel (HVOF) method highlights the fact that wear processes are influenced by the coating microstructure and the testing conditions [7, 8].

Other scientists claim that hot rolled steel plates such as 65Mn and 60Si2Mn coated with WC10Co4Cr showed reduced porosity, denser microstructure, minimal carbon evolution, improved adhesion strength and increased wear resistance [7].

At the same time, it has been established that wear of WC10Co4Cr coatings occurs when the surface of tungsten carbide (WC) particles are destroyed and exfoliated, while the CoCr binder phase undergoes microdestruction, forming grooves and microcracks that propagate until particle exfoliation leads to the formation of pits.

However, researchers such as Cheng et al. found that chromium oxide Cr_2O_3-based coatings with higher titanium oxide TiO_2 concentrations, known for their moderate hardness and good toughness, produced using the athmospheric plasma spray (APS) thermal method exhibit a denser microstructure and improved corrosion resistance in three different solutions such as HCl, NaCl, and NaOH. There is also a risk that ceramic coatings based on pure chromium oxide Cr_2O_3, due to their brittleness, may suffer from poor adhesion, delamination and porosity caused by insufficient particle melting [9, 10, 11, 12]. It has been established that dense TiO_2, which is part of chromium oxide Cr_2O_3, refines the grain size and fills intergranular voids, thus increasing the internal density of the composite coating [13].

In a study of high-temperature oxidation processes in CoCrNi alloys, Park et al. observed significant formation of spinel oxides, $CoCr_2O_4$ and $NiCr_2O_4$, in the outer oxide layer during oxidation.

Solution of the examined problem

To improve the quality of the working bodies of agricultural harrow discs, three types of coatings are applied to the active areas of the discs:

- W_2C/WC12Co (Metco71NS);
- Cr_2O_3-4SiO_2-3TiO (Metco136F);
- Co25.5Cr10.5Ni7.5W0.5C (Metco45CNS).

The experimental coatings were deposited using a Sulzer Metco 9MCE deposition system operating with Ar (5.3 bar, 45 NLPM) and H_2 (3.5 bar, 7.0 NLPM). After mechanical grinding and intensive sandblasting, samples with plasma spray thermal depositions on active areas of harrow discs were tested. Experimental setup includes a rotating support, an automated arm connected to a Sulzer 9MB spray gun, and a sample holder [14].

Powders for spraying the active areas of the harrow discs were produced by company Oerlikon Metco.

Concave and convex parts of harrow discs were coated using the atmospheric plasma spray (APS) thermal deposition method (fig.1).

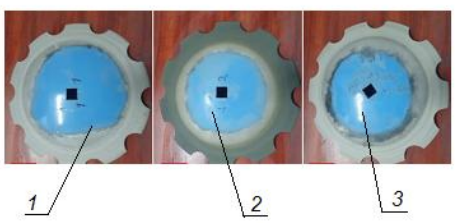


Figure 1. Convex part of experimental discs with coatings:
1 - Sample 1; 2 - Sample 2; 3 - Sample 3.

Before tribological testing, a series of tests were carried out to analyze the surface of the coated samples, using the following equipment [14, 15]:

- scanning electron microscopy (FEG Thermo Fisher - Quattro C, 2024);
- energy-dispersive X-ray spectroscopy (EDX - Bruker, X-Flash detector);
- panalytical equipment X-ray diffraction (XRD-Panalytical equipment).

The tests on the three already mentioned harrow disc samples were carried out using a CETR UMT-2 microtribometer for standard scratch and microhardness testing, connected to a computer (fig.2).

The following requirements apply to sample dimensions:

1) indentation and microscratch tests: 10 mm in width and 20 mm in length;
2) wear and friction tests:
   - for linear table: 10-20 mm in width and 20-30 mm in length,
   - for rotational table: disc with 12 to 65 mm in diameter,
   - pin specimen with 6.35 mm in diameter and 20-30 in length - for upper drive/force sensor.

All samples must have a thickness of maximum 5 mm.

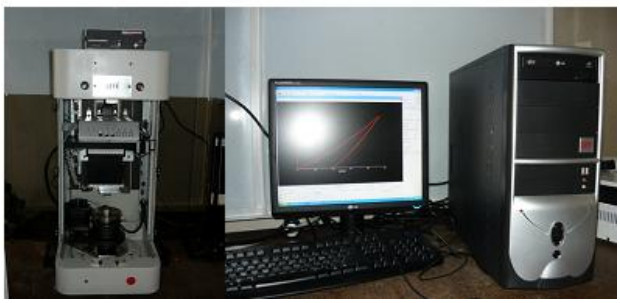


Figure 2. The CETR UMT-2 tribometer for standard scratch and microhardness testing, connected to a computer.

The CETR UMT-2 tribometer (fig.2) was used to analyze and conduct the standard tests of the following tribological processes [14, 15, 16]:

- study of wear processes and determination of friction coefficients at micro and nanometric scales in rotational motion for studied materials;
- study of the microscratch resistance of the material superficial layers;
- microindentation tests to determine the material microhardness and Young modulus.

The values of vertical and friction forces that can be measured between 0.1 mN and 20.0 N and resolution between 1 μN and 1mN, depending on the force sensors. The CETR UMT-2 tribometer (fig.2) covers the following force ranges: 0.1 mN-10 mN, 5 mN-500 mN and 0.2 N-20 N.

Microindentation test methodology. According to ASTM E18-05 standard, for the determination of Rockwell hardness the indentation test consists of 2 main stages [17]:

1) an initial pre-loading stage with a force of up to 10% of the maximum test force;
2) a loading stage with a force of up to 450 N, depending on the force range of the force sensor on which the indentation test is performed.

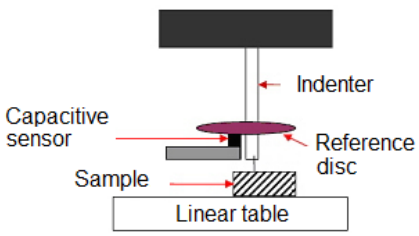


Figure 3. Schematic representation of the positioning of the capacitive sensor under the reference disc

First of all, it is necessary to set up the CETR UMT-2 tribometer to perform the microindentation test. To perform the microindentation test on the tribometer, the linear table is mounted on which the sample and the capacitive sensor support for recording the distance traveled by the indenter in the vertical direction are fixed (fig.3). For that, a two-kilogram force sensor is used, to which the rigid support in which the indenter support system is mounted is fixed by means of two screws.

A metal disk, called a reference disk, is fixed between the indenter support system and the indenter, under which the capacitive sensor is placed to record the vertical displacement of the indenter.

For a correct measurement of the indenter displacement, the capacitive sensor must be positioned as close as possible to the indenter, the entire circumference of the sensor must be covered by the reference disk, and the distance between the upper surface of the capacitive sensor and the reference disk must be 220-230 μm, in order not to exceed the sensor's working range of maximum 254 μm. If the capacitive sensor is positioned too close to the reference disc, there is a risk that the reference disc will hit the sensor (Fig.4).

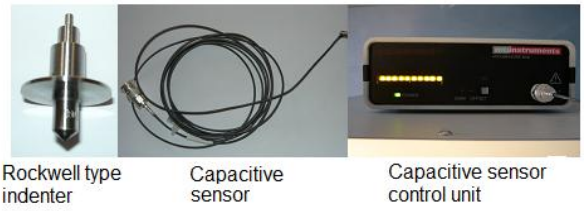


Figure 4. Main elements of the CETR UMT-2 tribometer for microindentation testing

The indenter used for this test has a conical shape at an angle of 120º, with a rounded diamond tip with a radius of 200 μm.

The capacitive sensor is attached to the support system that is mounted on the horizontal table (fig.4) and it is connected to the control unit, which is connected to the CETR tribometer [16].

The hardness measured by the indentation process is defined as the average contact pressure and is given by the relationship:

$$H_{IT} = \frac{F_{\max}}{A_P} \qquad (1)$$

where: F_{max} - the maximum force, N;
A_P - the projection of the contact area at this force, m^2.

Rezults and discussion

In order to determine the main material parameters such as substrate adhesion, coefficient of friction (COF), Young's modulus (modulus of elasticity), stiffness and hardness a tribological analysis was carried out (fig.5).



Figure 5. Conducting tribological tests in the laboratory of Technical University „Gheorghe Asachi", Iasi, Romania

The micro-scratch test was conducted to determine the friction coefficient, calculated as the ratio between the horizontal force F_x(N) and the applied loading force of 10 N, F_z(N) [14, 16].

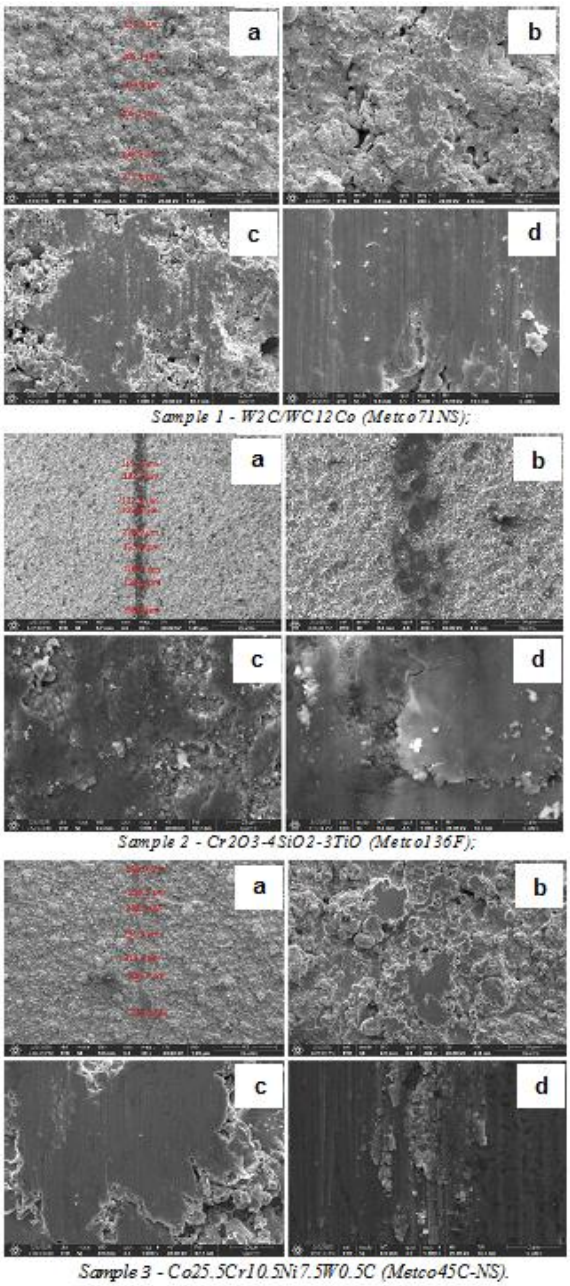


Figure 6. *Scratch analysis of the surface of samples: a) 50X; b) 200X; c) 1000X; d) 5000X.*

Figure 6 illustrates the scratch behavior and the size of the marks left by the indenter on the coated surface. In all three cases, the substrate was not reached, however, microcracks and detachment of the superficial surface layer were observed.

Table 1. *Results of tribological tests - scratch analysis*

	Sample	Determined mechanical properties			
		Coefficient of friction (COF)	Young's Modulus, GPa	Stiffness, N/µm	Hardness, GPa
1	*Sample 1* P1 - Metco 71NS	0.4105	23.988	2.482	1.143
2	*Sample 2* P2 - Metco 136F	0.5425	53.102	4.478	1.635
3	*Sample 3* P3 - Metco 45C NS	0.5059	37.679	3.672	1.255
4	Base Material	0.1394	42.964	4.393	1.131

To determine the COF coefficient, which was calculated using formula (1), a micro-scratch test was carried out. As a result, the average scratch width was: for Sample 1 - 227 µm, for Sample 2 - 124 µm, and for Sample 3 - 232 µm.

The values obtained as a result of scratch analysis for all three studied layers and the base material are presented in Table 1. Based on the data presented in Table 1, diagrams of the main material parameters such as the coefficient of friction (CF), Young's modulus, stiffness and hardness for coated samples and the base material were constructed and are presented in figures 7-10.

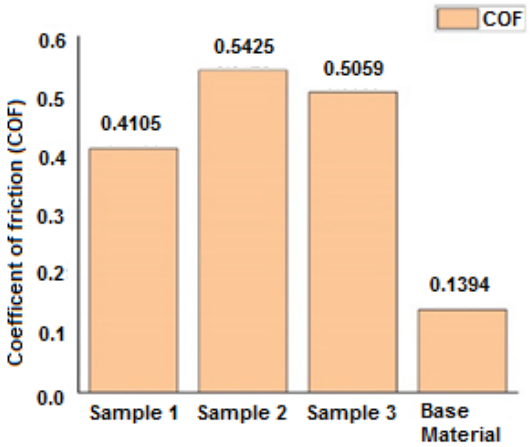


Figure 7. Apparent coefficient of friction (COF) of coated samples and the base material

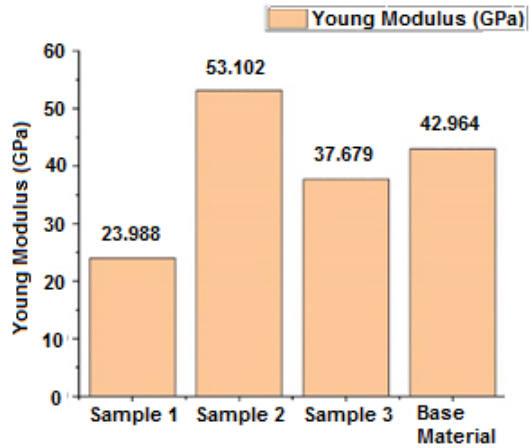


Figure 8. Young's modulus of coated samples and the base material

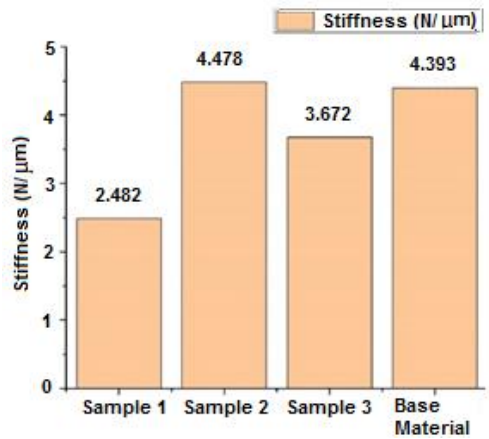


Figure 9. Stiffness of coated samples and the base material

Analysis of the tribological test results presented in fgures 7–10 for all three categories of tested samples coated by plasma spray thermal method and the base material shows that the deposition of

Sample 2, which contains ceramic compounds of chromium, silicon and titanium oxides (Cr_2O_3-$4SiO_2$-3TiO), led to a higher coefficient of friction, Young's modulus, stiffness and hardness, compared to the other two coatings.

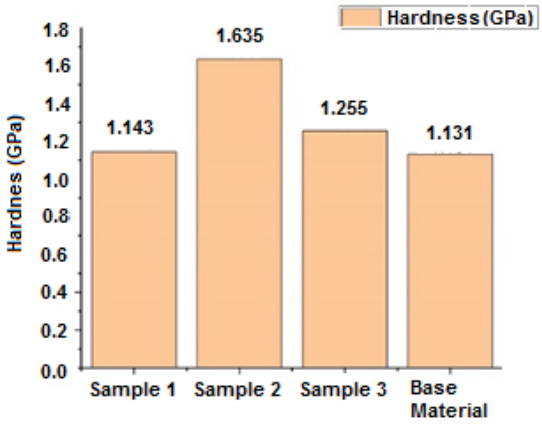


Figure 10. Hardness of coated samples and the base material

It is necessary to mention that in the case of stiffness, the highest and closest results were obtained for Sample 2 and the Base Material, the results being within the limits of the admissible error. Sample 1 recorded poor results for Young's modulus, stiffness and hardness, but for the coefficient of friction the result was better compared to the base material.

Conclusions

1. The morphological analysis revealed a rough and porous surface with some unmelted particles and small cracks of the coatings of the following samples (Sample 1 - W_2C/WC12Co (Metco71NS), Sample 2 - Cr_2O_3-$4SiO_2$-3TiO (Metco136F) and Sample 3 - Co25.5Cr10.5Ni7.5W0.5C (Metco45C-NS)) deposited on the active area of the harrow discs using atmospheric plasma spray thermal deposition. Tribological analysis of the coated samples was followed by Scratch analysis of the surface of samples.

2. To determine the coefficient of friction (COF), a micro-scratch test was performed, as a result of which the average scratch width was: for Sample 1 - 227 µm, for Sample 2 - 124 µm and for Sample 3 - 232 µm.

3. The scratch behavior, as well as the size of the indentation marks on the coated surface in all three cases, showed that the substrate was intact, but microcracks and delamination of the superficial layer were observed.

4. Sample 2, with Cr_2O_3-$4SiO_2$-3TiO (Metco136F) coatings deposited on the active area of the harrow discs using the atmospheric plasma spray thermal deposition showed the highest values among all studied coatings for coefficient of friction, Young's modulus, stiffness and hardness.

Acknowledgments

This work and research were supported by a grant from the Romanian Ministry of Education and Research, CNCS-UEFISCDI, project number PN-IV-P8-8.3-ROMD-2023-0108, within the PNCDI IV.

References

1. BARZEGAR, M., HASHEMI, S., NAZOKDASTB, H. Evaluating the draft force and soil-tool adhesion of a UHMW-PE coated furrower. In: Soil Tillage Res., Vol. 163, 2016. pp. 160-167.

2. MUNTEANU, C., MELNIC, IU., ISTRATE, B., HARDIMAN, M., GAIGINSCHI, L., LUPU, F., ARSENOAIA, V., CHICET, D., ZÎRNESCU, C., BADIUL, V. Comprehensive Review of Improving the Durability Properties of Agricultural Harrow Discs by Atmospheric Plasma Spraying (APS). In: *Coatings* 2025, *15*(6), 632.
https://doi.org/10.31399/asm.cp.itsc2025p0508

3. NATSIS, A., PETROPOULOS, G., PANDAZARAS, C. Influence of local soil conditions on mouldboard ploughshare abrasive wear. In: Tribol. Int., Vol. 41, 2008. pp. 151-157.

4. MELNIC, IU. Studiul teoretic al organelor de lucru de tip cuţit-disc ale maşinilor agricole. In: Agricultural Science, Issue 2, Chişinău: UASM, 2016. pp. 31-35. ISSN 1857-0003.

5. ŢENU, I., MELNIC, IU., ROŞCA, R, CÂRLESCU, P. Research on the impact of tillage operations for autumn wheat crop set up over some soil properties. In: Agricultural Science, Issue 2, Chişinău: UASM, 2018, pp.122-127, ISSN 1857-0003.
https://press.utm.md/index.php/as/issue/view/2018-2/full-issue

6. KUMARI, K., ANAND, K., BELLACCI, M., GIANNOZZI, M. Effect of microstructure on abrasive wear behavior of thermally sprayed WC-10Co-4Cr coatings. In: Wear, Vol. 268, 2010. pp. 1309-1319.
https://doi.org/10.1016/j.wear.2010.02.001

7. NIE, H., LI, Z., ZHOU, H., WU, J., WEN, G., LI, Y. Study on the wear resistance and mechanism of HVOFsprayed WC10Co4Cr coatings. In: Surface and Coatings Technology, Vol. 494, Part 1, 2024. pp. 131-136.

8. VASHISHTHA, N., KHATIRKAR, R., SAPATE, S. Tribological behaviour of HVOF sprayed WC-12Co, WC-10Co-4Cr and Cr3C2-25NiCr coatings. In: Tribol. Int., Vol. 105, 2017. pp. 55-68.
https://doi.org/10.1016/j.triboint.2016.09.025

9. CHENG, X., PENG, S., ZHOU, J., Zhu, Z. Influence of TiO_2 nano particles on the resistance to corrosion and mechanism of Cr_2O_3, Rare Met. Mater. Eng., Vol. 41, 2012. pp. 319-322.

10. LI, N., LI, G., WANG, H., KANG, J., DONG, T., WANG, H. Influence of TiO_2 content on the mechanical and tribological properties of Cr_2O_3-based coating. Mater Des, Vol. 88, 2015. pp. 906-914.
https://doi.org/10.1016/j.matdes.2015.09.085.

11. MANSHOR, H., AZHAR, A., RASHID, R., SULAIMAN, S., ABDULLAH, E., AHMAD, Z. Effects of Cr_2O_3 addition on the phase, mechanical properties, and microstructure of zirconia-toughened alumina added with TiO_2 (ZTA–TiO2) ceramic composite. In: Int Jounal Refract Met Hard Mater, Vol. 61, 2016. pp. 40-45.
https://doi.org/10.1016/j. ijrmhm.2016.08.005

12. VENTURI, F., PULSFORD, J. HUSSAIN, T. A novel approach to incorporate graphene nanoplatelets to Cr2O3 for low-wear coatings. Mater Lett, 2020. p. 276.
https://doi. org/10.1016/j.matlet.2020.128283

13. GRIMM, M., CONZE, S., BERGER, L., THIELE, S., LINDNER, T., LAMPKE, T. Microstructures and property profiles of atmospheric plasma sprayed $(Al,Cr,Ti)_2O_3$ solid solution coatings. Surf Coat Technol, 2023. p. 457.
https://doi.org/10.1016/j. surfcoat.2023.129309

14. MUNTEANU, C., ISTRATE, B., LUPU, F., BENCHEA, M., MELNIC, IU., VIŞANU, V. Increasing the Mechanical Characteristics of the Disc Harrow Component by APS Thermal Coatings. In: Thermal Spray 2025: Proceedings from the International Thermal Spray Conference May 6-8, 2025; Vancouver, Canada. Vancouver: Published Online: May 05 2025, Paper No: itsc2025fm01, pp. iii-v; 3 pages. pp. 508-514.
https://doi.org/10.31399/asm.cp.itsc2025p0508

15. CRETU, S., BENCHEA, M., IOVAN-DRAGOMIR, A. On basic reference rating life of cylindrical roller bearings. J. Balk. Tribol. Assoc., Vol. 21, 2016, pp. 820-830.

16. MUNTEANU, C., MELNIC, IU., ISTRATE, B., LUPU, F., VIŞANU, V., BADIUL, V., ZÎRNESCU, C. Study of harrow discs coated by plasma-thermal method. In: International Scientific Journal "Mechanization in agriculture & Conserving of the resources", Issue 2, 2025. pp.46-48. ISSN print 2603-3704, ISSN web 2603-3712.
https://stumejournals.com/am.htm

17. CETR UTM: Multi-specimen Test System. Hardwear Instalation and Applications Manual. Center for Tribology. 1715 Dell Ave, Campbell CA 95008, USA. 2009. 89 p.

Application of single-point incremental forming with industrial robot arm to analyze the impact of system stiffness on forming precision

Kosma Knap, Konrad Perzynski, Lukasz Madej

Faculty of Metals Engineering and Industrial Computer Science, AGH University of Krakow, Mickiewicza 30 av., 30-059 Krakow, Poland

knap@agh.edu.pl

Abstract: *Single-point incremental forming (SPIF) eliminates dedicated forming dies, enabling flexible and cost-effective production of complex thin-walled metallic components suitable for prototyping and low-batch manufacturing. This work develops and tests a robotic SPIF workstation using a Kawasaki RS030N industrial robotic arm to evaluate how system stiffness affects geometric accuracy. The research setup development includes a rigid forming table, a universal forming tool, and dedicated software for toolpath generation, robot communication, and parameter management. Experimental tests on aluminium and steel sheets of varying thicknesses assess the role of mechanical stiffness in maintaining dimensional accuracy. This foundational study completes the SPIF process chain—from toolpath generation and trajectory verification through forming trials and precision analysis—establishing a basis for future robotic additive forming systems aligned with Industry 4.0 principles.*

Keywords*: SPIF, ROBOTIC ARM, INDUSTRY 4.0*

1. Introduction

Single-point incremental forming (SPIF) is a flexible sheet metal forming technology that uses a simple tool, connected to a CNC machine or robotic arm, to progressively deform sheet material along a controlled trajectory. Unlike conventional stamping, which requires expensive forming dies, SPIF eliminates tooling costs and enables rapid conversions between different geometries. The process is ideal for prototyping and small-batch production of thin-walled components, with applications in aerospace, biomedical, and automotive industries [1-5].

The industrial applications of SPIF technology are varied and include products such as biomedical implants, parts for renovating vintage cars or architectural cladding. These components often feature complex, non-standard geometries that would not be economically attractive to produce using conventional stamping methods.

In the SPIF process, a forming tool performs precise, pre-programmed movements along a defined trajectory to incrementally deform the sheet part. The sheet is rigidly clamped to a forming table using various frame and clamp configurations, unlike the stamping process, where specialized dies are required for each new geometry. If necessary, additional tools can be used, such as support plates (to control wall thickness reduction) or auxiliary forming tools (to form complex shapes) [6,7] (Fig. 1).

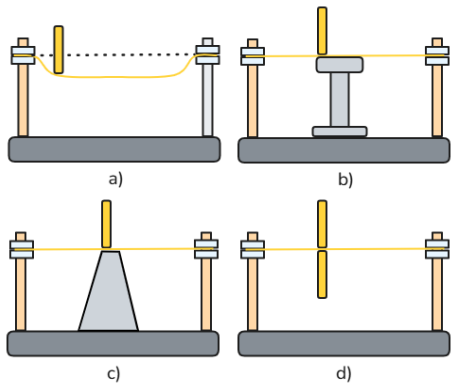


Fig. 1 *SPIF process variants: a) standard SPIF process with tool trajectory; b) SPIF with backing plate; c) SPIF with monolithic matrix; d) SPIF with two forming tools.*

The classical SPIF process has been adapted in this work for conducting preliminary research on the use of robotic arms in the process and for designing a research station.

2. Preliminary assumptions of the process and designed tooling

2.1 Experimental stand design

Two robotic platforms were used in the study: initially, a semi-industrial configuration with a Dobot M1 Pro arm for preliminary testing, followed by an industrial Kawasaki RS030N arm for industrial-scale production trials. This two-stage approach enabled iterative refinement of trajectory-planning algorithms and process parameters.

A modular forming stand was assembled, comprising: (i) a rigid steel frame (60mm × 60mm × 6mm) profiles for the support; 100mm × 40mm × 6mm profiles for the frame, bolted to an aluminum working table with M14 anchors; (ii) forming tools made of NC11LV tool steel (length 145mm, diameter 10mm, tip radius 5mm); (iii) a forming table for sheets up to 500mm × 500mm with an adjustable configuration of 200mm × 200mm.

The forming tool was heat-treated (hardening at 1020°C, tempering at 525°C/120min) to achieve 60HRC hardness, ensuring wear resistance and dimensional stability. Final polishing minimized tool-material friction and eventually improved surface quality of the formed component.

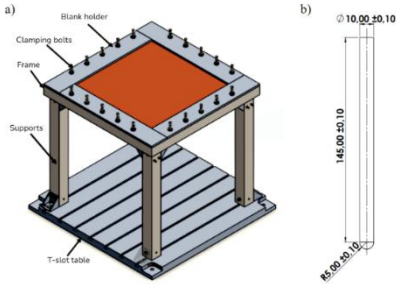


Fig. 2 *Experimental stand concept: a) 3D isometric view of modular forming table; b) forming tool technical drawing with dimensions.*

2.2 Control software and process management

A custom control application using Python and the Tkinter library was then developed, enabling trajectory generation, robot interface management, and parametric optimization. The software architecture supports two operating modes: real-time TCP/IP communication for the Dobot M1 Pro platform and generation of KIDE-compatible files for the Kawasaki RS030N system. The integrated visualization and simulation function allows for offline process verification, minimizing the number of trial and error iterations. Fig. 3 presents the graphical user interface for the developed robot control software.

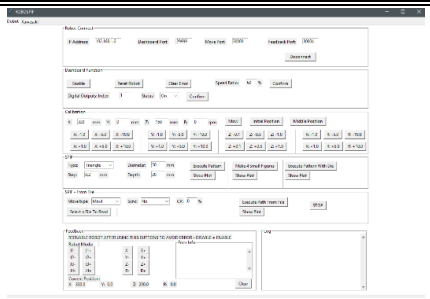


Fig. 3 *Control software interface: main dashboard showing calibration, parameters, and tool path visualization.*

3. Results of the conducted experiments

3.1 Experimental procedure

The initial objectives focused on confirming the assumptions regarding trajectory planning and algorithm reliability. The Dobot M1 Pro configuration was tested by producing complex copper and brass parts while monitoring the quality of the pressed elements and identifying movement irregularities.

Testing results on copper (M1Ez4) and brass (M63z4) thin sheet plates with a thickness of 0.1mm are summarized in Fig. 4. These samples exhibit successful pyramid-shaped and conical embossments, characterised by consistent deformation properties.

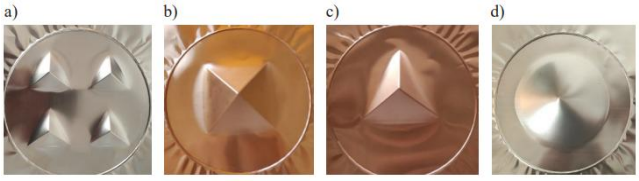


Fig. 4 *Representative test samples formed with Dobot M1 Pro: a) multi-stage brass formation; b) and c) copper pyramidal geometries; d) brass cone configuration.*

After successful verification of the algorithm using a semi-industrial platform, the experiments were transferred to a Kawasaki RS030N industrial arm. Subsequent tests evaluated the repeatability of the trajectory after scaling the dimensions to match the geometry of the production station, while also assessing the capabilities of handling materials with increased thickness and hardness.

The SPIF execution sequence, including parameter definition, path optimization, and part generation, is shown in Fig. 5.

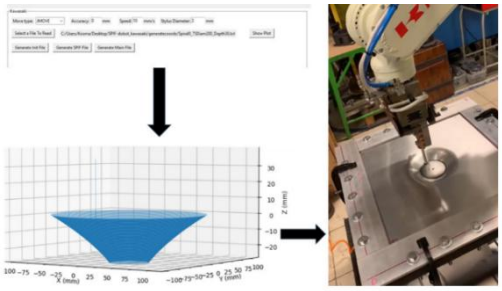


Fig. 5 *Schematic of SPIF process showing parameter input, path visualization, and forming execution.*

3.2 System stiffness and dimensional accuracy

A prototype part was produced from a full-scale aluminum sheet (500mm × 500mm) of 1050 alloy with a thickness of 1 mm. As shown in Fig. 6, the process proceeded correctly, and no forming defects in the form of cracks or large deviations from the designed shape were observed. Minor surface irregularities resulting from the tool movement and pressure on the material are visible on the part surface. More detailed determination of surface roughness level requires further testing, which is planned for subsequent project stages. At present, rigid steel frame architecture minimized elastic deformation, while M14 anchors prevented experimental stand deflections.



Fig. 6 *Effects of prototype part forming: a) view from bottom; b) view from top; c) close-up of the wall.*

The 60HRC hardness achieved through heat treatment ensured consistent tool performance. The modular design enabled successful scaling from semi-industrial to industrial platforms, validating trajectory algorithms across different systems. Tests confirm the process produces parts free from defects such as cracks.

SPIF offers advantages over stamping for prototypes: eliminated die costs and rapid geometry transitions. However, long forming times render it unsuitable for high-volume scenarios.

4. Conclusion

The developed robotic SPIF experimental stand demonstrates feasibility for small-batch production with validated reliability. The two-stage experimental approach confirmed that system stiffness directly influences geometric precision. Key contributions include: (i) a modular, scalable robotic platform; (ii) integrated control software; (iii) validation of defect-free forming.

Future developments include: (i) workpiece heating systems (~300°C) for refractory alloys; (ii) sensor-integrated real-time monitoring; (iii) robot compliance compensation algorithms. The experimental stand provides the basis for the development of incremental robotic manufacturing in line with Industry 4.0 principles.

6. References

[1] Cheng Z., Li Y., Xu C., Liu Y., Ghafoor S., Li F., Incremental sheet forming towards biomedical implants: a review, Journal of Materials Research and Technology, vol. 9, iss. 4, 2020, s. 7225–7251, https://doi.org/10.1016/j.jmrt.2020.04.096.

[2] Prasad, R., Oraon, M., & Sharma, V. (2024). Application of Artificial Intelligence in Single Point Incremental Forming for Surface Roughness Prediction. 12. https://doi.org/10.37591/JoPC

[3] Kumar, A. (2024). Critical state-of-the-art literature review of surface roughness in incremental sheet forming: A comparative analysis. Applied Surface Science Advances, 23. https://doi.org/10.1016/j.apsadv.2024.100625

[4] Duflou, J. R., Habraken, A. M., Cao, J., Malhotra, R., Bambach, M., Adams, D., Vanhove, H., Mohammadi, A., & Jeswiet, J. (2018). Single point incremental forming: state-of-the-art and prospects. In International Journal of Material Forming (Vol. 11, Issue 6, pp. 743–773). Springer-Verlag France. https://doi.org/10.1007/s12289-017-1387-y

[5] Nasulea D., Oancea G., Incremental deformation: A literature review, MATEC Web of Conferences, 8th International Conference on Manufacturing Science and Education – MSE 2017 "Trends in New Industrial Revolution", vol. 121, 2017, 03017, https://doi.org/10.1051/matecconf/201712103017.

[6] Trzepieciński T., Oleksik V., Pepelnjak T., Najm S.M., Paniti I., Maji K., Emerging trends in single point incremental sheet forming of lightweight metals, Metals, vol. 11(8), 2021, 1188, https://doi.org/10.3390/met11081188.

[7] Vanhulst M., Lee Y., Steinfels D., Bremen T., Perzyński K., Vanhove H., Ambrogio G., Breaz R.E., Buffa G., Cao J., Conte R., de Napoli L., Fratini L., da Terrence Fu X., Gagliardi F., Gralha M., Kang P., Kuczek Ł., Kumar A.S., Kunke A., Leonhardt A., Li Y., Li Z., Licari R., Long H., Wei Wen Low D., Racz S.G., Scholz P., Silva M.B., Song S., Weise D., Żaba K., Zhu H., Bailly D., Banu M., Madej L., Duflou J.R., ESAFORM benchmark 2024: study on the geometric accuracy of a complex shape with single point incremental forming, International Journal of Material Forming 18(72), 2025, https://doi.org/10.1007/s12289-025-01928-1.

Thermoeconomic Analysis of an Organic Rankine Cycle for LNG Cold Energy Utilization

Josip Grbac[1], Paolo Blecich[1,*], Mateo Kirinčić[1], Igor Bonefačić[1]
Faculty of Engineering, University of Rijeka, Croatia[1]
* paolo.blecich@riteh.uniri.hr

Abstract: *Liquefied natural gas (LNG) has become a crucial source of energy supply security amid growing geopolitical tensions in recent years. During LNG regasification, a substantial amount of cold energy is released, and typically wasted into seawater. The cold-energy potential of LNG during regasification and warming from −161 °C to +15 °C at 80 bar is 750 kJ/kg, while the associated exergy potential is 400 kJ/kg. This paper investigates the potential for converting LNG cold energy into electricity through a cryogenic binary cycle. The results indicate that integrating an ORC system into the LNG regasification process can yield substantial energy and economic benefits while reducing the thermal waste at regasification terminals. The recoverable power per 1 kg/s of LNG is 90 kW/(kg/s) for a single-pressure ORC configuration using ammonia as the working fluid. The levelized cost of electricity (LCOE) is 45 €/MWh while specific installation costs (SIC) are 2225 €/kW for a brownfield retrofit project on an existing regasification unit. This research confirms that the application of innovative cryogenic cycles enables a more sustainable and efficient use of the LNG supply chain, contributing to the decarbonization of the energy sector.*

Keywords*: LIQUEFIED NATURAL GAS (LNG); COLD ENERGY UTILIZATION; THERMOECONOMIC ANALYSIS; ORGANIC RANKINE CYCLE (ORC).*

1. Introduction

Liquefied natural gas (LNG) is expected to play a crucial role in facilitating the global transition towards renewable energy systems. LNG can be transported via sea routes between producers and consumers, enabling flexible worldwide energy supply. The current global LNG liquefaction capacity stands at 670 billion cubic meters (bcm) per year, equivalent to approximately 490 million tonnes annually (MTPA), by the end of 2024. This capacity is expected to expand significantly as new projects become operational. Between 2025 and 2030, more than 300 bcm (220 MTPA) of new export capacity is anticipated to commence operations [1]. From January to October 2025, final investment decisions (FIDs) for LNG reached record levels, totaling 96 bcm/year of new liquefaction capacity worldwide, with the United States accounting for 83 bcm/year of this growth [2].

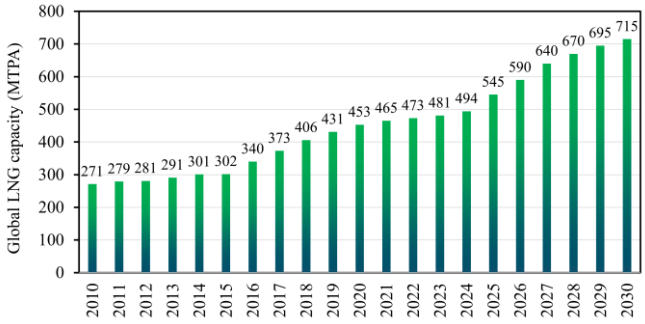


Fig. 1. *Global LNG capacity: recorded data (2010-2024) and forecasted data (2025-2030)*

Natural gas liquefaction is a highly energy-intensive process, requiring 0.3–0.4 kWh of compression or turbine power to produce 1 kg of LNG [3]. The cooling energy required to liquefy natural gas from +15 °C to −161 °C at 1 atm amounts to 850 kJ/kg [4]. Prior to regasification, LNG is generally pressurized to 60–80 bar, matching the inlet pressure of natural gas transmission networks. During warming from −161 °C to +15 °C at 80 bar, LNG possesses a cold-energy potential of 750 kJ□ □ /kg$_{LNG}$, corresponding to an exergy potential of 400 kJ/kg$_{LNG}$. Assuming an average cryogenic power plant exergy efficiency of 40% [5], the current global LNG regasification capacity (490 Mt$_{LNG}$/year) represents a theoretical electricity generation potential of approximately 2.5 GW.

LNG cold energy can be harnessed for multiple applications, including power generation, air separation, seawater desalination, refrigeration and cooling, and cryogenic CO_2 capture [6]. Other uses involve district cooling, food preservation, and data center cooling, or as an auxiliary cooling source in air separation, hydrogen, and ammonia liquefaction processes. Hybrid systems integrating several cold-energy applications can substantially reduce the overall power and cooling requirements at LNG regasification terminals [7].

Among these applications, power generation is the most extensively studied. Commonly investigated cycles include direct expansion (DE) [8–9], the Kalina cycle [10], the Brayton cycle [11], and the Organic Rankine Cycle (ORC) [12–13]. The ORC is generally preferred due to its technological maturity, ease of integration, and proven effectiveness in converting low-temperature heat sources such as geothermal [14], solar [15], and seawater energy [16]. LNG cold-energy utilization through ORC systems is analogous to Intermediate Fluid Vaporizer (IFV) configurations, both employing seawater as a heat source to vaporize an intermediate fluid. However, unlike IFVs that discharge LNG cold energy into the ambient, ORCs recover part of this energy as useful work. The research on systems and components for cold energy and waste heat utilization is gaining growing attention [17–20], as they recover valuable energy that would be otherwise wasted into the ambient, increasing the overall energy efficiency and reducing greenhouse gas emissions from the industry.

The vaporization pressure of LNG affects the selection of the working fluid and ORC configuration. The recoverable power per 1 kg/s of LNG is 100–120 kW/(kg/s) for single-stage, 130–150 kW/(kg/s) for two-stage, and up to 225 kW/(kg/s) for double two-stage parallel ORC systems [21]. Direct expansion and cryogenic turboexpanders achieve 150–165 kW/(kg/s) [22]. The recoverable power increases with the heat source temperature, ranging from 158 kW/(kg/s) at 25 °C to 249 kW/(kg/s) at 85 °C [23]. Daniarta et al. [24] reviewed cryogenic power systems including ORC, Brayton, Kalina, DE, and supercritical CO_2 cycles, reporting efficiencies of 6.5–48% for ORC, 30–73% for Brayton, 24–48% for DE, and 32–45% for Kalina and SCO_2 cycles, depending on the working conditions.

ORC systems cover a wide range of power outputs: micro-ORC units (1–50 kW) are used for small-scale waste-heat recovery; small-scale units (50–500 kW) are applied to geothermal, biomass, and solar-thermal sources; medium-scale systems (0.5–5 MW) serve industrial and CHP applications [25]; while large-scale ORCs can reach 50 MW, particularly in geothermal power plants [26].

Recent advances in LNG cold-energy power generation have aimed to enhance the performance of the traditional Rankine cycle. Several studies [27] improved thermal efficiency using internal heat recuperators, which preheat the working fluid via turbine outlet vapor. Others [28] employed flash tanks or fluid mixtures to better match the temperature profile of the heat source. Further efficiency

gains have been demonstrated by combining multiple Rankine loops in series or parallel, as well as through cascade and multi-stage cycle configurations [29].

Previous studies have mostly focused on the thermodynamic optimization, while fewer studies have addressed the economic performance of ORC systems for LNG cold energy utilization.

Tsougranis and Wu [30] examined a two-stage cryogenic ORC integrated into an LNG-powered vessel. Using ethylene (C_2 H_4) as the working fluid, the study reported a specific investment cost (SIC) in the range of 4300-4900 US$/kW. The corresponding LCOE was calculated as 42-48 US$/MWh, assuming a 5% discount rate, 20-year lifetime, and 8,000 operating hours per year. Other studies of LNG cold-energy utilization found higher cost levels when additional subsystems or storage components are integrated. For instance, Zheng et al. [31] assessed small-scale LNG cold-energy power generation systems and reported LCOEs in the range of 90-110 US$/MWh along with an exergy efficiency of 48-55%. Similarly, Wang et al. [32] evaluated a 10 MW LNG cold energy power plant with liquid air energy storage and calculated an LCOE of 100 US$/MWh at an exergy efficiency of 63%. Other studies report LCOE values in the range of 100-300 US$/MWh [33] for more complex ORC configurations and partial-load operation.

The literature overview revealed that the economic performance of ORC systems for LNG cold energy utilization is still lacking. To fill this research gap, the present study carries a thermo-economic assessment that evaluates both the energy and economic performance of ORC systems for LNG cold energy utilization.

2. Methodology

The ORC system for LNG cold energy utilization is modelled as a single-pressure configuration with ammonia as the working fluid, as shown in Figure 2. The system integrates three main circuits: the ORC working-fluid loop (purple line), the LNG circuit (green line), and the seawater circuit (blue line). This system simultaneously generates power through the ORC turbine by utilizing the temperature difference between warm seawater and cold LNG, and regasifies LNG, using the ORC condenser and the afterheater as heat sources [34]. The integration maximizes exergy utilization by recovering LNG cold energy while minimizing environmental impact and improving overall thermal efficiency.

The ORC loop converts low-temperature thermal energy into mechanical power, which is then converted to electricity via a generator. LNG acts as the cold source for condensation, while seawater provides the heat source for evaporation and preheating of the ORC working fluid.

Seawater, driven by a seawater pump, transfers heat to the ORC working fluid in the preheater, ④ → ⑤. The preheated ORC fluid continues to the evaporator, where it absorbs additional heat from seawater and becomes dry or superheated vapor, ⑤ → ①. The ORC vapor expands through a turbine, ① → ②, producing mechanical work that drives a generator to produce electricity. The exhaust vapor from the turbine is condensed using LNG as the cooling medium. Here, the LNG absorbs heat and is vaporized, while the ORC working fluid is condensed into liquid, ② → ③. The condensed ORC fluid is pressurized by a feed pump, ③ → ④, and sent back to the preheater, completing the closed cycle.

On the LNG side, a cryo pump pressurizes the LNG from the LNG tank pressure (1 bar) to the pressure at the inlet of the natural gas transmission network (70 bar), ⑥ → ⑦. The LNG passes through the condenser, ⑦ → ⑧, absorbing heat from the ORC fluid and vaporizing. The partially vaporized LNG then flows through an LNG afterheater, ⑧ → ⑨, where it is further warmed by seawater to meet delivery conditions.

The physical properties of LNG are assumed to be equivalent to those of pure methane (CH_4), while the effects of heavier hydrocarbon components are neglected. The physical properties of seawater were approximated by those of freshwater for simplification, and all thermophysical calculations were performed using the REFPROP v10.0 database. The heat balance equations for the evaporator, the preheater and the condenser are:

$$\dot{Q}_{EV} = \dot{m}_{sw} \cdot c_{sw} \cdot \Delta T_{sw} = \dot{m}_{ORC}\left(h_1 - h_5\right) \tag{1}$$

$$\dot{Q}_{PH} = \dot{m}_{sw} \cdot c_{sw} \cdot \Delta T_{sw} = \dot{m}_{ORC}\left(h_5 - h_4\right) \tag{2}$$

$$\dot{Q}_{C} = \dot{m}_{ORC}\left(h_2 - h_3\right) = \dot{m}_{LNG}\left(h_8 - h_7\right) \tag{3}$$

The turbine and the feed pump power are calculated as follows:

$$\dot{W}_{T} = \dot{m}_{ORC}\left(h_1 - h_2\right) = \dot{m}_{ORC}\left(h_1 - h_{2s}\right)\eta_{T} \tag{4}$$

$$\dot{W}_{FP} = \dot{m}_{ORC}\left(h_4 - h_3\right) = \frac{\dot{m}_{ORC}\left(h_{4s} - h_3\right)}{\eta_{FP}} \tag{5}$$

The net thermal efficiency of ORC system is determined as the ratio between the net power output and the total heat flow to the preheater and evaporator:

$$\eta_{th,net} = \frac{\dot{W}_{net}}{\dot{Q}_{EV} + \dot{Q}_{PH}} = \frac{\dot{W}_{T} - \dot{W}_{FP}}{\dot{m}_{ORC} \cdot (h_1 - h_4)} \tag{6}$$

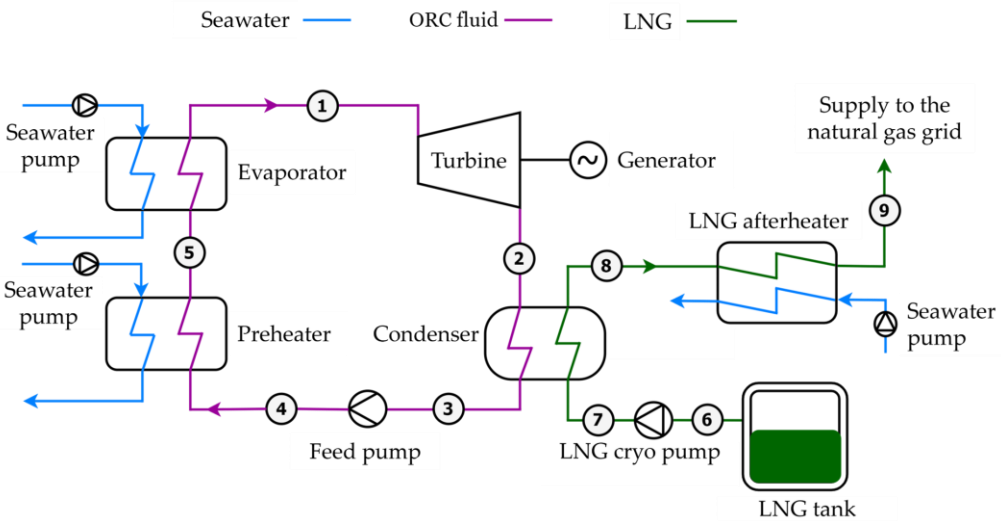


Fig. 2. *Configuration of the single-pressure ORC power plant for LNG cold energy utilization*

The levelized cost of electricity (LCOE) is the net present value of all the power plant lifetime costs divided by the net present value of all the electricity produced. It is the ratio between the total discounted costs, including capital investment, operation and maintenance, and the total discounted electricity generation. The LCOE indicates the minimum electricity price at which the project breaks even economically.

$$LCOE = \frac{C_{CAP} + \sum_{t=1}^{t=N} C_{O\&M,t}\left(1+e\right)^t \Big/ \left(1+r\right)^t}{\sum_{t=1}^{t=N} E_{net}(1-d)^t} \quad (7)$$

The present value of the project capital cost is the product of the annuity and the project lifetime:

$$C_{CAP} = A \cdot T = C_{project} \frac{r \cdot (1+r)^T}{(1+r)^T - 1} \cdot T \quad (8)$$

Table 1. lists the assumed values of the economic parameters necessary for calculating the LCOE. Total project costs are estimated from the major equipment costs (turbines, pumps, heat exchangers, compressors, tanks). The equipment costs are increased using multiplication factors, which account for direct (site preparation, assembly, piping, insulation, electrical, sensors, controls, etc.) and indirect costs (transport, contingencies, fees).

$$C_{project} = \sum_{i}^{N} \underbrace{C_{EQ}\left[1 + f_{TM} + f_{aux}\right]}_{\text{referent equipment costs}} \underbrace{\left(\frac{CEPCI_{2024}}{CEPCI_{ref}}\right)}_{\text{cost index correction}} \quad (9)$$

Table 1: *Assumed values for the economic analysis of the ORC system*

Economic parameter	Value
Discount rate (real value), *r*	7%
Price escalation rate, *e*	4%
Capacity degradation rate, *d*	1%
Project lifetime, *T*	25 years
Contingencies and fees, f_{TM}	+20% (f_{TM} = 0,20)
Auxiliary costs, f_{AUX}	+60% (f_{AUX} = 0,60)
Annual O&M costs	130 €/kW
Annual operating hours	7000 h

The equipment costs (C_{EO}) are estimated using cost correlations available in the literature [35]. Because these correlations were derived from historical cost data, the calculated equipment costs are updated to present-day values by applying the appropriate cost index adjustment ($CEPCI_{2024}/CEPCI_{ref}$). The Chemical Engineering Plant Cost Index (CEPCI) is published monthly by the Chemical Engineering magazine [36] and tracks the cost of equipment, materials, labor, and construction in chemical process plants.

Specific installation cost (SIC) indicates how much is the capital investment per unit of net power output:

$$SIC = \frac{C_{project}}{\dot{W}_{net}} \quad (10)$$

3. Results and discussion

The LNG cold energy power plant achieves a net power output of 6.7 MW using ammonia as the working fluid and for an LNG regasification capacity of 400,000 m^3/h (75.5 kg/s). The specific net power output is 90 kW/(kg/s) net power output is achieved for a condensation pressure of 0.156 bar, equivalent to a condenser temperature of -65 °C, as shown in figure 3. The seawater temperature is 20 °C while the minimum pinch point temperature difference in the evaporator and condenser is 10 °C. The LNG enters the condenser at -161 °C and leaves with a temperature of -75 °C. The LNG is heated up to +15 °C in the afterheater, which is the temperature at the inlet of the natural gas transmission network.

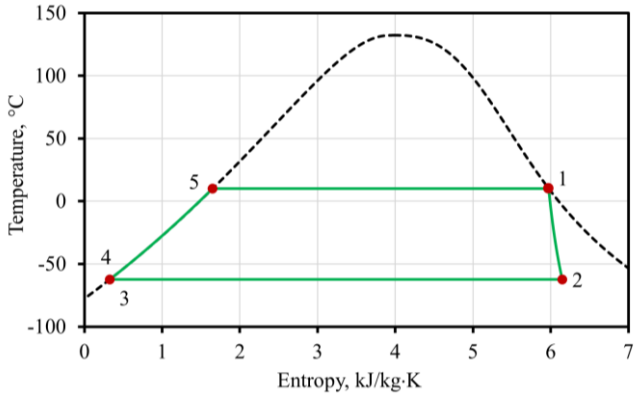


Fig. 3. *Temperature-entropy chart of LNG cold energy power plant using ammonia as the working fluid*

The net power output exhibits a characteristic peak for all fluids (ethane, propane, pentane, ammonia and carbon dioxide), as shown in figure 4. As the saturation temperature in the condenser decreases from −30 °C toward cryogenic temperatures, the net power initially increases, reaches a maximum at −65 °C, and then declines. In general, lowering the condenser saturation temperature increases the enthalpy drop in the turbine, however, this also reduces the mass flow rate of the ORC working fluid. The net thermal efficiency of the ORC system ranges between 21% for ammonia and 15% for carbon dioxide.

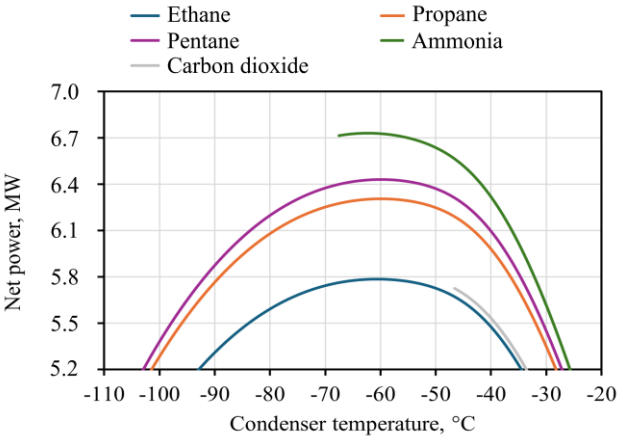


Fig. 4. *Power output as function of the condensation temperature, regasification capacity of 400,000 m^3/h*

The SIC are estimated at 2225 €/kW for a brownfield project, i.e., an LNG cold-energy power plant integrated into an existing regasification terminal. The LCOE is estimated at 45 €/MWh, which is comparable to the most recent economic indicators of other renewable energy power plants [37], as reported in table 2.

Table 2: *Comparison of the ORC power plant for LNG cold energy utilization with other renewable power plants*

Power plant type	**SIC (€/kW)**	**LCOE (€/MWh)**
Biofuels	3016	80
Geothermal	3734	55
Hydro	2108	52
Solar PV	642	40
CSP	3422	85
Wind onshore	967	31
Wind offshore	2652	73
LNG cold energy	2225	45

4. Conclusions

The present study evaluated a single-pressure ORC integrated with LNG regasification and demonstrated that significant power can be recovered from LNG cold energy. Using ammonia as the working fluid, the system achieves a net power output of 6.7 MW at an LNG flow rate of 75.5 kg/s, corresponding to a specific power output of 90 kW/(kg/s). Maximum performance occurs at a condenser saturation temperature of approximately −65 °C, with a thermal efficiency of about 21%. Economically, the specific installation cost is estimated at 2225 €/kW for a brownfield installation, while the LCOE of 45 €/MWh positions LNG cold-energy recovery as cost-competitive against other mature renewable energy power generation options.

Future research should investigate multi-stage and recuperated ORC configurations, different working fluids and their mixtures, and integrated systems combining power, desalination, and cold-storage functions. Broader economic analyses including carbon pricing and market uncertainties could further support the transition of LNG terminals toward efficient and low-carbon operation.

Acknowledgements

This research was supported by European Union – Next Generation EU, within the University of Rijeka projects UNIRI-IZ-25-186: "Sustainable Energy Solutions for Emission Reduction in Maritime Transport and Ports" and UNIRI-IZ-25-271: "Fuel Cell Integration into Ship Power Systems".

5. References

1. International Energy Agency (IEA), *Gas 2025: Analysis and forecasts to 2030* (IEA, Paris, 2025).
2. International Energy Agency (IEA), *Global LNG Capacity Tracker* (IEA, Paris, 2025).
3. IEAGHG, *Techno-Economic Evaluation of CO_2 Capture in LNG Plants*, 2019/07 (IEA Greenhouse Gas R&D Programme, Cheltenham, United Kingdom, 2019).
4. A. Hajji, M. Chahartaghi, M. Kahani, "Thermodynamic analysis of natural gas liquefaction process with propane pre-cooled mixed refrigerant process (C3MR)," *Cryogenics* 103, 102978 (2019).
5. F. Chen, W. Zhang, J. Xuan, J. Cai, H. Zhang, "Analysis of LNG cold energy utilization and regasification process for a gas turbine power plant integrated with a novel polygeneration process," *Applied Thermal Engineering* 258(Part C), 124738 (2025).
6. M.H. Noor Akashah, N.E. Mohammad Rozali, S. Mahadzir, P.Y. Liew, "Utilization of cold energy from LNG regasification process: A review of current trends," *Processes* 11, 517 (2023).
7. M. Zonfrilli, M. Facchino, R. Serinelli, M. Chesti, M. De Falco, M. Capocelli, "Thermodynamic analysis of cold energy recovery from LNG regasification," *Journal of Cleaner Production* 420, 138443 (2023).
8. M.R. Gómez, R.F. García, J.R. Gómez, J.C. Carril, "Review of thermal cycles exploiting the exergy of LNG in the regasification process," *Renewable and Sustainable Energy Reviews* 38, 781–795 (2014).
9. A. Franco, C. Casarosa, "Thermodynamic analysis of direct-expansion configurations for electricity production by LNG cold energy recovery," *Applied Thermal Engineering* 78, 649–657 (2015).
10. L.A. Prananto, I.N. Zaini, B.I. Mahendranata, F.B. Juangsa, M. Aziz, T.A.F. Soelaiman, "Use of the Kalina cycle as a bottoming cycle in a geothermal power plant: Case study of the Wayang Windu geothermal power plant," *Applied Thermal Engineering* 132, 686–696 (2018).
11. G. Angelino, C.M. Invernizzi, "The role of real gas Brayton cycles for the use of liquid natural gas physical exergy," *Applied Thermal Engineering* 31, 827–833 (2011).
12. J. Bao, Y. Lin, R. Zhang, X. Zhang, N. Zhang, G. He, "Performance enhancement of a two-stage condensation combined cycle for LNG cold energy recovery using zeotropic mixtures," *Energy* 157, 588–598 (2018).
13. J. Wajs, D. Mikielewicz, B. Jakubowska, "Performance of the domestic micro-ORC equipped with a shell-and-tube condenser with minichannels," *Energy* 157, 853–861 (2018).
14. A. Arbula Blecich, P. Blecich, "Thermoeconomic analysis of subcritical and supercritical isobutane cycles for geothermal power generation," *Sustainability* 15, 8624 (2023).
15. F.A. Boyaghchi, A. Sohbatloo, "Assessment and optimization of a novel solar-driven natural gas liquefaction system based on a cascade ORC integrated with linear Fresnel collectors," *Energy Conversion and Management* 162, 77–89 (2018).
16. F. Xue, Y. Chen, Y. Ju, "Design and optimization of a novel cryogenic Rankine power generation system employing binary and ternary mixtures as working fluids based on the cold exergy utilization of liquefied natural gas (LNG)," *Energy* 138, 706–720 (2017).
17. P. Blecich, T. Senčić, I. Wolf, I. Bonefačić, "Numerical investigation of heat and mass transfer inside a wet cooling tower," *Tehnički glasnik* 12(3), 131–138 (2018).
18. A.S. Bisht, V.S. Bisht, P. Bhandari, K.S. Rawat, T. Alam, P. Blecich, "The use of a vortex generator for the efficient cooling of lithium-ion batteries in hybrid electric vehicles," *Processes* 11, 500 (2023).
19. P. Blecich; J. Batista; M. Kirinčić; A. Trp; K. Lenić, "Numerical study of heat transfer and fluid flow in the offset strip-fin heat exchanger: a fin-by-fin analysis," *International Communications in Heat and Mass Transfer* 154, 107434 (2024).
20. M. Kirinčić, T. Fadiga, B. Delač, "Influence of fin spacing and fin height in passive heat sinks: numerical analysis with experimental comparison," *Applied Sciences* 15, 11410 (2025).
21. J. Bao, T. Yuan, L. Zhang, N. Zhang, X. Zhang, G. He, "Comparative study of liquefied natural gas (LNG) cold energy power generation systems in series and parallel," *Energy Conversion and Management* 184, 107–126 (2019).
22. A. Franco, C. Giovannini, "Optimal design of direct expansion systems for electricity production by LNG cold energy recovery," *Energy* 280, 128173 (2023).
23. K. Kim, U. Lee, C. Kim, C. Han, "Design and optimization of cascade organic Rankine cycle for recovering cryogenic energy from liquefied natural gas using binary working fluid," *Energy* 88, 304–313 (2015).
24. S. Daniarta, P. Błasiak, P. Kolasiński, A.R. Imre, "Sustainability by means of cold energy utilization-to-power conversion: A review," *Renewable and Sustainable Energy Reviews* 205, 114833 (2024).
25. R. Loni, G. Najafi, E. Bellos, F. Rajaee, Z. Said, M. Mazlan, "A review of industrial waste heat recovery system for power generation with organic Rankine cycle: Recent challenges and future outlook," *Journal of Cleaner Production* 287, 125070 (2021).
26. C. Wieland, C. Schifflechner, F. Dawo, M. Astolfi, "The organic Rankine cycle power systems market: Recent developments and future perspectives," *Applied Thermal Engineering* 224, 119980 (2023).
27. J. Krail, G. Beckmann, F. Schittl, G. Piringer, "Comparative thermodynamic analysis of an improved ORC process with integrated injection of process fluid," *Energy* 266, 126352 (2023).
28. Z. Wang, R. Zhang, H. Shao, T. Nie, "Thermodynamic performance of flash-dual-pressure organic Rankine cycle system for power generation from hot dry rock geothermal resources," *Applied Thermal Engineering* 281(Part 2), 128603 (2025).
29. R. Ma, Y. Lu, X. Yu, B. Yang, "Thermodynamic, economic, and environmental multi-criteria optimization of a multi-stage Rankine system for LNG cold energy utilization," *Modelling* 6, 45 (2025).
30. E. L. Tsougranis, D. Wu, "A feasibility study of Organic Rankine Cycle (ORC) power generation using thermal and cryogenic waste energy on board an LNG passenger vessel," *International Journal of Energy Research* 42, 3121–3142 (2018).
31. X. Zheng, J. Zhang, Y. Li, H. Yuan, C. Guo, S. Zhao, N. Mei, "Sustainably harnessing of LNG cold energy for power generation and wastewater desalination," *Energy* 326, 136341 (2025).
32. C. Wang, J. Zhang, N. Sun, "Performance study and economic analysis of LNG cold energy integrated with liquid air energy storage: Simulation and experiment," *Energy* 339, 139050 (2025).
33. R. Li, F. Tang, J. Pan, Q. Cao, T. Hu, K. Wang, "Energy integration of LNG cold energy power generation and liquefied air energy storage: Process design, optimization and analysis," *Energy* 321, 135513 (2025).
34. J. Grbac, *Thermodynamic analysis of the gasification process of liquefied natural gas for possible electricity generation*, Master Thesis, Faculty of Engineering, University of Rijeka, Croatia, 2025. Available online: https://repository.riteh.uniri.hr/en/object/riteh:5391
35. G. Towler, R. Sinnott, *Chemical Engineering Design: Principles, Practice and Economics of Plant and Process Design*, 3rd ed., Butterworth-Heinemann (Elsevier), Oxford, UK (2021).
36. Chemical Engineering Magazine: Essentials for the CPI Professional, Available at: https://www.chemengonline.com/
37. International Renewable Energy Agency (IRENA), *Renewable Power Generation Costs in 2024*, Abu Dhabi, UAE (2025). Available online: https://www.irena.org/Publications/2025/Jun/Renewable-Power-Generation-Costs-in-2024

Optical and microstructural properties of hybrid sol–gel derived ZrO_2–Al_2O_3–Sm_2O_3 coatings on glass for photovoltaic applications

Shaban Uzun[1], Stancho Yordanov[1], Mariela Dimitrova[2], Vladimir Petkov[1], Tatyana Ivanova[3], Angel Velikov[1]
[1]Bulgarian Academy of Sciences, Institute of Metal Science, Equipment and Technologies with Hydro- and Aerodynamics Centre "Acad. Angel Balevski", 67 "Shipchenski prohod" Blvd., 1574 Sofia, Bulgaria,
[2.] Institute of Electrochemistry and Energy Systems "Academician Evgeni Budevski at the Bulgarian Academy of Sciences", 1574 Sofia, Bulgaria
[3.] Central Laboratory of Solar Energy and New Energy Sources, Bulgarian Academy of Sciences, Tzarigradsko chaussee 72, 1784 Sofia, Bulgaria
e-mail: stancho14@abv.bg

Abstract: *This work presents an overview of sol–gel-derived oxide materials and their relevance to optical, photonic and photovoltaic applications, followed by an experimental study of ZrO_2–Al_2O_3–Sm_2O_3 thin films deposited on glass substrates. Historical developments of the sol–gel process, beginning with early investigations on silica gels in the 19th century, are outlined together with advancements in optical glasses, anti-reflective coatings, and rare-earth-doped systems. Recent progress in functional materials—including boron-, tellurium- and rare-earth-containing glasses, luminescent oxide systems, and sol–gel-derived zirconia-based coatings—is discussed to highlight their structural, optical and radiation-shielding capabilities.*

In the present study, multilayer ZrO_2–Al_2O_3–Sm_2O_3 coatings were prepared via the sol–gel method combined with dip-coating, and subsequently thermally treated at 420 °C. Optical characterization (UV–VIS–NIR) revealed changes in transmittance and reflectance linked to film composition and thickness, while X-ray diffraction confirmed their predominantly amorphous structure at the applied heat-treatment temperature. SEM and EDS analyses provided insight into surface morphology and elemental distribution within the films. The results demonstrate that increasing Al_2O_3 content influences coating porosity and thickness, while Sm_2O_3 contributes luminescent functionality and potential reduction of optical reflection in key solar spectral regions. These findings indicate that ZrO_2–Al_2O_3–Sm_2O_3 thin films are promising candidates for protective and functional coatings in photovoltaic applications, where enhanced light harvesting and improved surface properties are essential.

Keywords: SOL-GEL, DIP COATING, ZrO_2–Al_2O_3–Sm_2O_3, PHOTOVOLTAIC APPLICATIONS

1. Introduction

The sol–gel method for processing inorganic ceramic and glass materials began to be investigated as early as the mid-19th century with the works of Ebelmen and Graham on silica gels, who discovered that the hydrolysis of tetraethyl orthosilicate (TEOS) under acidic conditions forms glass-like SiO_2. The early gels enabled the production of fibers, optical lenses and composites, but the long drying time limited their technological application.

At the end of the 19th and the beginning of the 20th century, gels attracted the attention of chemists due to Liesegang rings and the periodic crystallization phenomena studied by renowned scientists such as Ostwald and Lord Rayleigh [1]. The role of glass in solar energy production and its development for various applications is discussed. The requirements for glass composition to achieve higher solar light transmittance are described. Anti-reflective coatings that improve the efficiency of crystalline silicon photovoltaics are considered. The applications of coated glasses in thin-film photovoltaics are also presented, showing the most intensive emission band at 598 nm, including transparent conductive layers and the benefits of high-resistance transparent coatings. Subsequently, the use of mirror coatings for concentrating solar systems is analyzed, as well as the main manufacturing and technological challenges related to materials and coatings [2,3].

Boron-, tellurium- and rare-earth-based glasses are widely used in optical applications and as shielding materials for γ-rays and neutrons. The addition of SrO modifies the structural and optical properties of these glasses, including density, optical band gap, and absorption characteristics of Sm^{3+} ions, as well as parameters affecting radiation attenuation. Further optimization of SrO content can improve shielding ability by reducing the half-value layer (HVL) and increasing the linear attenuation coefficient, making these glasses suitable for modern optical and radiation-protection applications [4].

Photoluminescence in the UV–VIS region represents a sensitive method for studying the structure and optical properties of glasses and glass-ceramics. Fluoride, phosphate and silicate glasses with high intrinsic UV transparency and chemical purity have been investigated, doped with active luminescent ions with different electronic configurations (s^2: As^{3+}, Sb^{3+}, Sn^{2+}, Pb^{2+}; d^0: Ti^{4+}, Nb^+, Mo^{6+}, Ta^{5+}, W^{6+}; d^{10}: Zn^{2+}, Ag^+ and Cu^+; d^5: Mn^{2+}; f^h such as Sm^{3+}, Eu^{3+}, Eu^{2+}, Tb^{3+}). These ions exhibit diverse photoluminescent activity depending on their electronic structure and the local symmetry of the surrounding environment. The thermal transformation of glass into glass-ceramic changes the coordination and distribution of active centers, leading to variations in the intensity and spectral range of emission, with recorded blue, green and red emissions and lifetimes from 1 μs to 25 ms, confirming the potential of these materials for photonic and optoelectronic applications [5].

Thin ZrO_2–Y_2O_3 (YSZ) sol–gel films with 3–12 mol% Y_2O_3 were produced and characterized. All films crystallized in the cubic phase, even at Y_2O_3 contents that do not stabilize this phase in bulk ZrO_2. With increasing Y_2O_3 content, the refractive index slightly increased, while optical absorption, extinction coefficient, hardness and elastic modulus decreased, due to reduced crystallinity and greater lattice distortion in ZrO_2 [6,7].

In the present study, micro-organized multilayer coatings based on $ZrO_2/Y_2O_3/Al_2O_3$ were developed and characterized, obtained by combining the sol–gel method with dip-coating. The influence of Al_2O_3 content (0–20%) on the morphology, structure and physicochemical properties of the coatings was investigated. The optimized procedure developed by the research team enabled the preparation of transparent, stable and coatable solutions even at high concentrations of the aluminum oxide phase. The results show that increasing Al_2O_3 content leads to increased thickness and porosity of the coatings, as well as a higher dimensionless flow parameter (J), indicating a larger amount of deposited material. It was also found that the microstructure and crystallinity of the substrates have a limited influence on film thickness but not on porosity. The obtained data outline the potential of these systems for use as protective or functional oxide coatings with controllable properties [8,9].

In the ZnO–B_2O_3–SiO_2–Al_2O_3 system, glasses produced via melt-quenching at different ZnO/SiO_2 ratios (from 5.4 to 1.4) were investigated to determine their effect on glass formation and crystallization behavior. Thermal treatments up to 1050 °C showed sequential crystallization of $Zn_3(BO_3)_2$, β- and α-willemite (Zn_2SiO_4), as well as the formation of gahnite ($ZnAl_2O_4$) at higher temperatures. The resulting materials exhibited bluish-white photoluminescence under λ_{ex} = 254 nm, making them potential candidates for photonic and optoelectronic applications [10].

.

1. Experimental procedures

For the synthesis, zirconyl chloride octahydrate ($ZrOCl_2 \cdot 8H_2O$), samarium oxide (Sm_2O_3), nitric acid (HNO_3), acetic acid (CH_3COOH), and distilled water were used. All reagents were of analytical grade and were used without further purification.

A total of 8.048 g of $ZrOCl_2 \cdot 8H_2O$ was dissolved in 35 mL of absolute ethanol C_2H_5OH (99.9%). The solution was homogenized by magnetic stirring for 1 h and then left to stand for an additional 2 h to ensure complete dissolution and stabilization at room temperature.

Sm_2O_3 (0.527 g) was added to 15 mL of deionized water. A total of 2.5 mL of concentrated HNO_3 was added to the suspension, ensuring its complete dissolution by converting Sm_2O_3 into $Sm(NO_3)_3$, resulting in a clear solution. The obtained transparent solution was used without further processing.

Al_2O_3 (0.255 g) was dispersed in 15 mL of deionized water, followed by the addition of 2.5 mL of HNO_3. The acid treatment improved the surface activity of the particles, facilitating the formation of a stable aqueous dispersion.

The precursors were combined in the following sequence: the $ZrOCl_2$ solution was mixed sequentially with the samarium nitrate solution and the Al_2O_3 dispersion under continuous stirring. To the resulting mixture, 3 mL of acetylacetone (AcAc) was added as a stabilizing agent, along with 2.5 mL of glacial acetic acid (AcOH) to adjust the acidity and stabilize the metal complexes. The final pH of the system was adjusted to 0.5, which prevented hydrolysis and precipitation of the highly charged metal ions and ensured a stable homogeneous precursor. All processes were carried out at room temperature. The resulting homogeneous mixture was left to age for 20 hours before use.

2. Results and Discussion

Optical characterization was performed with UV–VIS–NIR Shimadzu 3600 double-beam spectrophotometer in the spectral region of 280-1800 nm. The transmittance spectra were taken against air. The reflectance spectra were measured by using the specular reflectance attachment (5º incidence angle) and Al coated mirror as reference.

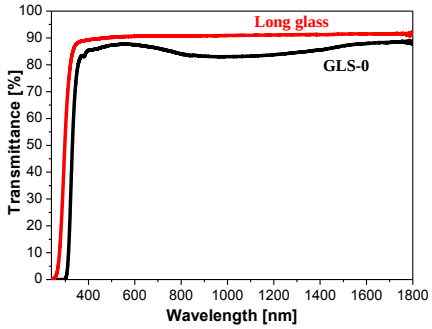


Figure 1. *The figure shows the transmission spectrum of a clean ZSA-0 substrate*

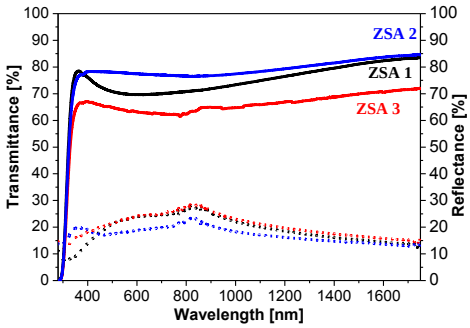


Figure 2. *The figure shows the transmission and reflectance spectrums of a samples: ZSA1, ZSA2, ZSA3*

An X-ray diffractometer with a Bragg-Brentano θ-2θ focusing system was used. The samples were examined at room temperature with Cu-Kα radiation (monochromatic radiation with wavelength λ = 154178Å) in the interval $20^o<2\theta<65^o$, at a step of 0.025 2θ for 10 seconds. A graphite monochromator was used for better peak resolution (better signal-to-noise ratio).

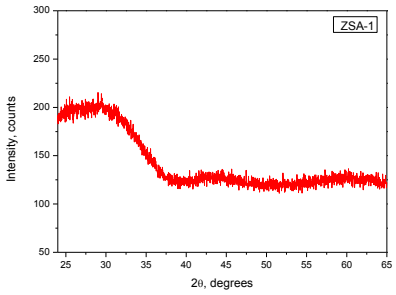


Figure 3. *The figure shows the X-ray diffractometer of ZSA1*

The X-ray diffraction patterns of ZSA1, ZSA2 and ZSA3 are of the same type - they show a typical amorphous state, i.e. at 420°C the temperature is the glass transition temperature.

The surface morphology of the samples was studied with the scanning electron microscopy technique, using the SEM unit Zeiss Evo 10 (Carl Zeiss Microscopy GmbH, Jena, Germany). Images were taken in secondary electrons mode with 25 keV accelerating voltage and no special coating on the samples. The chemical composition was investigated with energy dispersive spectroscopy (EDS) using a Zeiss SmartEDX probe, and the results were compiled with APEX software (version 1.5.0017).

The EDS analysis focused on the functional components of the ZrO_2–Al_2O_3–Sm_2O_3 system clearly reveals the presence of zirconium, aluminum, and samarium in the resulting coating. Zirconium is the dominant metallic element, with its content (14.41 wt%) confirming the successful formation and high concentration of the ZrO_2 phase within the sol–gel layer. Aluminum is detected at 0.45 wt%, which corresponds to the expected low Al_2O_3 content under the applied synthesis conditions. Samarium is identified at a mass fraction of 0.31 wt%, indicating uniform incorporation of Sm_2O_3 into the oxide network.

The presence of these three elements and their relative concentrations confirm that the functional ZrO_2–Al_2O_3–Sm_2O_3 system is successfully integrated into the sol–gel coating, forming a homogeneous and stable oxide layer.

”

The discussion includes: Optical Properties, Structural Analysis (XRD and Morphology and Elemental Composition (SEM/EDS) - shows the following&

1. Optical Properties

- The clean ZSA-0 substrate exhibits high optical transmittance in the 280–1800 nm range, confirming its suitability as a base for subsequent functional coatings.
- The coated samples ZSA1, ZSA2, and ZSA3 show varying degrees of changes in transmittance and reflectance, indicating that the optical properties depend on the composition and concentration of the added oxides (ZrO_2, Sm_2O_3, Al_2O_3).
- The observed decreases in transmittance at specific wavelengths are likely due to the formation of an amorphous oxide network and increased light scattering resulting from the nanostructured surface.

2. Structural Analysis (XRD)

- The diffraction patterns of samples ZSA1, ZSA2, and ZSA3 exhibit a typical amorphous profile, characterized by broad, weakly pronounced maxima and the absence of crystalline peaks.
- This confirms that the temperature of 420°C is below the crystallization threshold of the system and corresponds to the glass-transition region.
- The absence of crystalline phases indicates successful formation of a stable sol-gel amorphous oxide matrix, which is preferred for optical applications due to its low light-scattering properties.

3. Morphology and Elemental Composition (SEM/EDS)

- SEM measurements reveal a smooth and uniform surface without agglomerates or cracks, which is characteristic of well-formed sol-gel coatings.
- The EDS analysis of ZSA1 confirms the presence of all intentionally introduced elements — Zr, Sm, and Al — as well as the main components of the glass matrix (Si, O, Na, Ca, Mg).
- The high relative content of oxygen (≈59 wt%) and silicon (≈10 wt%) corresponds to the formation of a stable Si–O–Zr network.
- Zr (≈14.4 wt%) is the dominant metallic component, confirming the successful incorporation of zirconium into the coating structure.
- The presence of Sm, although in low concentration, demonstrates that the rare-earth element is evenly distributed within the resulting oxide system.
- The low carbon content indicates minimal residual organic material after heat treatment.

3. Conclusions

1. The obtained coatings are amorphous, optically active, and chemically homogeneous, demonstrating the effectiveness of the applied sol-gel procedure.

2.The combination of ZrO_2, Sm_2O_3, and Al_2O_3 results in stable and uniform oxide layers suitable for photovoltaic and photonic applications.

3.The optical analysis, XRD, and EDS results are mutually consistent and confirm the successful synthesis of the desired layers.

4.The coatings on glass substrates were prepared by sol-gel method using dipping technique. The present study characterizes self-cleaning thin films of ZrO_2, Al_2O_3 and Sm_2O_3 for photovoltaic applications.

5.This study investigates the optical and microstructural properties of ZrO_2–Al_2O_3–Sm_2O_3 coatings prepared by the sol–gel method and deposited on glass substrates for photovoltaic applications, as they enhance the efficiency of light-to-electricity conversion. The addition of Al_2O_3 improves the mechanical stability and interface adhesion, while Sm_2O_3 acts as a luminescent additive that modifies the spectral response and can reduce surface reflection at key solar wavelengths.

References:

1.L. L. Hench, J. K. West, The sol-gel process. Chemical Reviews, (1990), 90(1), 33-72.

2.Ganjoo, Ashtosh, et al. "Glass and coatings on glass for solar applications." *Springer Handbook of Glass*. Cham: Springer International Publishing, 2019. 1635-1676.

3.Biswas, Joydeb, et al. "Optical and luminescence properties of Sm_2O_3 doped SrO–PbO–ZnO–P_2O_5–TeO_2 glasses for visible laser applications." *Solid State Sciences* 129 (2022): 106910.

4.AL-GHAMDI, Hanan, et al. Strontium Oxide-Reinforced Borotellurite Glasses: Synthesis, Structure, and Optical Characteristics and γ-Ray and Neutron Attenuation Capability. *Journal of Electronic Materials*, 2024, 53.9.

5.EHRT, Doris. Photoluminescence in glasses and glass ceramics. In: *IOP Conference Series: Materials Science and Engineering*. IOP Publishing, 2009. p. 012001.

6.Diaz-Parralejo, Antonio, et al. "Optical and mechanical characterization of sol-gel thin films of ZrO2 stabilized with different Y_2O_3-doping mol%." *Ceramics International* 49.11 (2023): 19552-19555.

7.Fedorov, Pavel P., and Evgeniya G. Yarotskaya. "Zirconium dioxide. Review." *Конденсированные среды и межфазные границы* 23.2 (eng) (2021): 170-188.

8.Carrasco-Amador, Juan Pablo, et al. "Preparation and characterization of ZrO_2/Y_2O_3/Al_2O_3-based microstructured multilayer sol–gel coatings." *Ceramics International* 43.16 (2017): 14210-14217.

9.Díaz-Parralejo, Antonio, et al. "Mechanical properties and thermal shock in thin ZrO_2–Y_2O_3–Al_2O_3 films obtained by the sol-gel method." *Ceramics international* 47.1 (2021): 80-86.

10. Abdel-Hameed, Salwa AM; MARGHA, Fatma H. Preparation, crystallization and photoluminescence properties of un-doped nano willemite glass ceramics with high ZnO additions. *Optik*, 2020, 206: 164374.

Phenomena during liquid-phase assisted sintering in High-Entropy Ceramics with a Ni binder

Humeniak Mykola[1], Vedel Dmytro[1,2], Vronska Yuliia.[1], Zatsarna Oleksandra[1], Taran Serhii[3], Stasiuk Oleksandr.[1]

[1] G. V. Kurdyumov Institute for Metal Physics of the N.A.S. of Ukraine
[2]Frantsevich Institute for Problems in Materials Science, 3 Krzhizhanovsky St., 03142 Kyiv, Ukraine
[3]Interregional academy of personal management, Kyiv, Ukraine

E-mail: olek.stasiuk@gmail.com

Abstract: *This study investigates the mechanisms of liquid-phase assisted sintering in high-entropy ceramics (HECs) using a nickel binder. The research focuses on the densification process of (Ti, Zr, Hf, Nb, Ta)C-based cermets with 10 vol% Ni, and how pressure influence liquid-phase extraction. Results show that eutectic reactions between Ni and carbide phases was observed during liquid formation below 1400°C. Microstructural analysis reveals a nickel-rich matrix, solid solutions, and NbC-based carbide inclusions in the extracted drop. These findings provide insights into optimizing processing parameters for advanced HEC-based composites.*

Keywords: CERMETS, MICROSTRUCTURE, HIGH-ENTROPY CERAMICS, LIQUID-PHASE ASSISTED SINTERING

Introduction.

High-entropy ceramics (HECs) offer an excellent combination of hardness, wear resistance, and oxidation resistance compared to conventional single-phase ceramics. HECs can be classified into several categories, including high-entropy carbides, borides, oxides, and silicides [1-20]. The base line high-entropy carbide is (Ti, Zr, Hf, Nb, Ta)C, which have high mechanical properties at both room and elevated temperatures compared to single-phase carbides. Achieving full densification of HECs typically requires high sintering temperatures, around 2100–2300°C. However, two main approaches can be used to decrease the densification temperature: (i) the addition of refractory compounds such as SiC, and (ii) the indroduction of metals like Co, Ni, or their combinations.

The development of cermets with a hard HEC phase have several advantages, most notably a significant reduction in the densification temperature while retaining high mechanical properties. Nevertheless, due to the high contact angle between HECs and Fe, Co, or Ni, additional pressure is required to achieve a fully dense composite. Our previous work [21] has shown that applying a relatively low pressure (~10 MPa) can substantially increase the density of HEC cermets, whereas higher pressures (e.g., 15 MPa) may result in the extraction of liquid from the cermet. This liquid phase led to densification of the ceramics.

The aim of the present study is to investigate the nature of the liquid phase extracted during the densification of cermets based on (TiZrHfNbTa)C with a 10 vol% Ni binder, in order to better understand the phenomena occurring during liquid-phase assisted sintering.

Materials and experimental procedure.

The carbides powders were weighted in an equiatomic ratio and then mixed in acetone for 5 h by using the planetary mill. The (Ti, Zr, Hf, Nb, Ta)C powders were heating with heating rate 100 o C/min to 1800 o C in a vacuum and held 1 hour in heat resistance graphite furnace SSHVL-10 (IPMS, Ukraine). After first synthesis powders were ground and sifted through a sieve and mixed in acetone for 5 h by using the planetary mill. The second synthesis was carried out in the same condition. The powder size after second synthesis and grounding was ~ 2-4 mm.

The powder of HEC and metals were weighted in ratio 90 vol% HEC and 10 vol% Ni The powders were mixed in acetone during 5 h to obtain homogenous mixture.

Disk with a diameter of 30 mm was placed in a graphite die pre-coated with boron nitride for protection of the materials from direct interaction with the tools. Hot pressing was carried out in an SPD-120 apparatus (Frantsevich Institute for Problems in Materials Sciences, Ukraine (IPMS)). An induction-heating with heat rate 100°C/ min was set to achieve temperature of 1400-1550°C according to the piston movement during shrinkage. The initial load was 7 MPa and, once achieved the peak temperature, the load was increased to 5 or 30 MPa. The dwell at the maximum temperature was 15 min, the furnace was slowly cooled down to 1200°C to avoid crack formation.

The microstructure of the drop was investigated by scanning electron microscopy (SEM) on a MIRA 3 microscope (Tescan Co., Czech Republic) equipped with an energy diffraction spectroscope (EDS) (INCA X- Max, Oxford Instruments, Abingdon-on-Thames, UK).

Results and discussion.

The liquid phase sintering was the main mechanism of densification in cermets. It should be noted that there is melting in binary Ni-Single phase carbide system: (Ni-TaC)eutectic (Te=1340°C), (Ni-NbC) eutectic (Te=1320°C) , (Ni-HfC)eutectic (Te=1310°C), (Ni-WC)eutectic (Te=1300°C), (Ni-ZrC)eutectic (Te=1290°C), (Ni-TiC)eutectic (Te=1260°C).

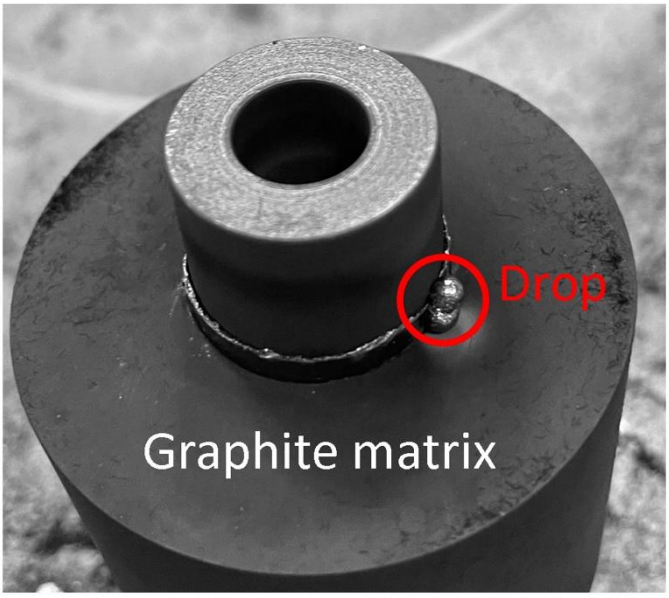


Fig. 1 *– The general view of the graphite matrix after densification of HEC-10 vol. % Ni system*

From this perspective, in the Ni/HEC (high-entropy ceramic) system, the formation of a liquid phase can be observed at temperatures below 1400°C. This is due to the eutectic reactions

between nickel and the various carbide components, which lower the melting point compared to the individual components.

The careful optimization of both temperature and pressure is necessary for achieving fully dense composite densification by hot pressing liquid-phase assistant sintering. Because these parameters critically influence the microstructure and properties of the final composite.

Among these factors, pressure stands out as one of the most significant variables affecting the microstructure. At low to medium pressures (5–10 MPa), the generated liquid phase tends to remain within the cermet matrix, increasing the densification rate.

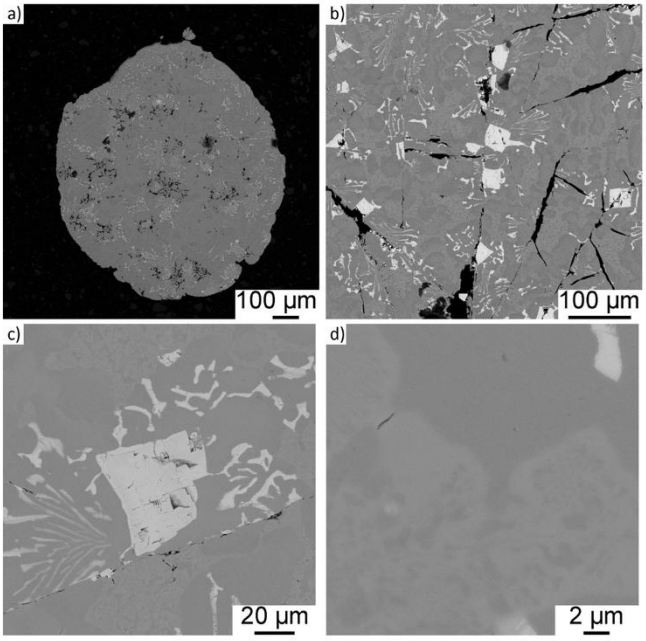


Fig. 2 *– The cross section of the drop that extract after densification in HEC-10 vol. % Ni system: general view (a), microstructure of the eutectics (b), microstructure of the NbC based and lamellar ZrC based crystal (c), microstructure of the Ni and Ni solid solution (d)*

However, as the pressure increases to around 15 MPa, the liquid phase begins to be expelled from the cermet, and at even higher pressures (30 MPa), it is completely extracted from the graphite die. This extraction process can alter the distribution of phases and may impact the overall mechanical properties of the material.

Simultaneously, overheating of the material during hot pressing can lead to pronounced grain growth. While the microstructure may remain homogeneous, the increase in grain size can negatively affect certain mechanical properties, such as hardness and toughness.

A cross-sectional analysis of a drop extracted after hot pressing in the HEC-Ni system (Fig. 2) reveals a complex phase composition. The droplet consists of pure nickel, a nickel solid solution with dissolved elements such as Zr, Ti, Hf, Nb, and Ta (Fig. 3), and various carbide phases. In the droplet, the metal and carbide phases form a eutectic microstructure, confirming the occurrence of eutectic reactions in the HEC-Ni system (Fig. 2b). The matrix is primarily composed of nickel and nickel-based solid solutions, while the carbide inclusions exhibit both lamellar and faceted morphologies.

Notably, the main carbide phase is based on NbC, which forms as a result of liquid-phase interactions during the crystallization process. The thin, lamellar crystals are enriched with Zr, Hf, and Nb. It is inferred that at approximately 1298°C, the liquid phase forms, and when a high additional load is applied, this liquid is forced through the powder compact and graphite die.

This liquid wets the powder surface and leads to its densification. The euctic nature of the droplet indicates that the initial stage of sintering involves the dissolution of carbide elements in the nickel, followed by their reprecipitation through the liquid phase.

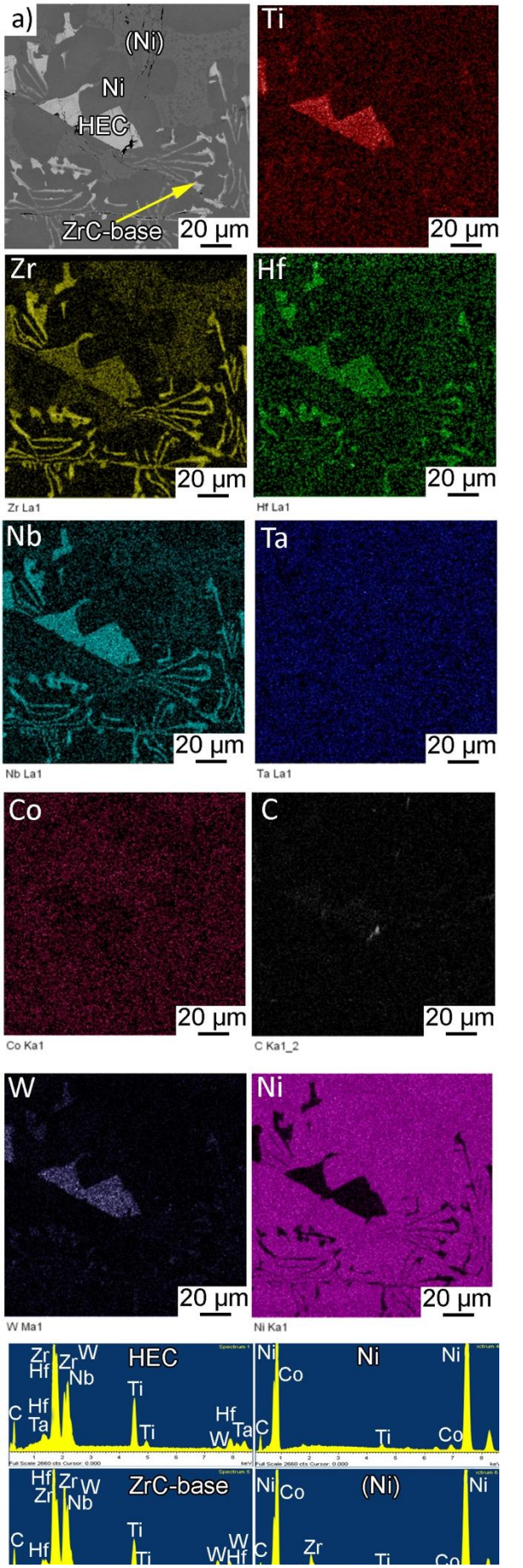


Fig. 3 *– The microstructure of the drop at high magnification with EDS map analysis and EDS spectrum of the separate phase*

The extracted liquid dissolves carbides, resulting in a supersaturated melt of these elements, which subsequently crystallizes to form a skeleton of carbide phases. This process significantly influences the thermal and chemical behavior of the material, as well as its final microstructure and properties.

Conclusions

1. Eutectic reactions between nickel and carbide phases in the Ni/HEC system was observed during HP sintering by investigation of the drop that extract.
2. The formed liquid wets the surfaces of the particle that increase the densification rate.
3. The liquid phase promotes the formation of a nickel-rich matrix, solid solutions, and NbC-based carbide inclusions. Careful control of temperature and pressure is essential for optimizing the microstructure and mechanical properties of advanced HEC-based composites.

References.

[1] P. Sarker et al., "High-entropy high-hardness metal carbides discovered by entropy descriptors," Nat Commun, vol. 9, no. 1, pp. 1–10, 2018, doi: 10.1038/s41467-018-07160-7.
[2] A. Sarkar, B. Breitung, and H. Hahn, "High entropy oxides: The role of entropy, enthalpy and synergy," Scr Mater, vol. 187, pp. 43–48, 2020, doi: 10.1016/j.scriptamat.2020.05.019.
[3] H.-R. Mao, E.-T. Dong, S.-B. Jin, X.-M. Qiu, and P. Shen, "Ultrafast high-temperature synthesis and densification of high-entropy carbides," J Eur Ceram Soc, vol. 42, no. 10, pp. 4053–4065, 2022, doi: https://doi.org/10.1016/j.jeurceramsoc.2022.03.054.
[4] J. Gild et al., "A high-entropy silicide: (Mo0.2Nb0.2Ta0.2Ti0.2W0.2)Si2," Journal of Materiomics, vol. 5, no. 3, pp. 337–343, 2019, doi: 10.1016/j.jmat.2019.03.002.
[5] M. H. Tsai and J. W. Yeh, "High-entropy alloys: A critical review," Mater Res Lett, vol. 2, no. 3, pp. 107–123, 2014, doi: 10.1080/21663831.2014.912690.
[6] Y. Zhang et al., "Fabrication of textured (Hf0.2Zr0.2Ta0.2Cr0.2Ti0.2)B2 high-entropy ceramics," J Eur Ceram Soc, vol. 41, no. 1, pp. 1015–1019, 2021, doi: 10.1016/j.jeurceramsoc.2020.08.071.
[7] J. Gild et al., "High-Entropy Metal Diborides: A New Class of High-Entropy Materials and a New Type of Ultrahigh Temperature Ceramics," Sci Rep, vol. 6, no. October, pp. 2–11, 2016, doi: 10.1038/srep37946.
[8] E. Castle, T. Csanádi, S. Grasso, J. Dusza, and M. Reece, "Processing and Properties of High-Entropy Ultra-High Temperature Carbides," Sci Rep, vol. 8, no. 1, Dec. 2018, doi: 10.1038/s41598-018-26827-1.
[9] L. Feng, W. G. Fahrenholtz, G. E. Hilmas, and Y. Zhou, "Synthesis of single-phase high-entropy carbide powders," Scr Mater, vol. 162, pp. 90–93, 2019, doi: 10.1016/j.scriptamat.2018.10.049.
[10] Y. Zhang et al., "Dense high-entropy boride ceramics with ultra-high hardness," Scr Mater, vol. 164, pp. 135–139, 2019, doi: 10.1016/j.scriptamat.2019.01.021.
[11] Y. Zhang et al., "Microstructure and mechanical properties of high-entropy borides derived from boro/carbothermal reduction," J Eur Ceram Soc, vol. 39, no. 13, pp. 3920–3924, 2019, doi: 10.1016/j.jeurceramsoc.2019.05.017.
[12] L. Feng, F. Monteverde, W. G. Fahrenholtz, and G. E. Hilmas, "Superhard high-entropy AlB2-type diboride ceramics," Scr Mater, vol. 199, p. 113855, 2021, doi: 10.1016/j.scriptamat.2021.113855.
[13] S. Failla, P. Galizia, S. Fu, S. Grasso, and D. Sciti, "Formation of high entropy metal diborides using arc-melting and combinatorial approach to study quinary and quaternary solid solutions," J Eur Ceram Soc, vol. 40, no. 3, pp. 588–593, 2020, doi: 10.1016/j.jeurceramsoc.2019.10.051.
[14] A. Sarkar et al., "High-Entropy Oxides: Fundamental Aspects and Electrochemical Properties," Advanced Materials, vol. 31, no. 26, 2019, doi: 10.1002/adma.201806236.
[15] Y. Qin et al., "High-entropy silicide ceramics developed from (TiZrNbMoW)Si2 formulation doped with aluminum," J Eur Ceram Soc, vol. 40, no. 8, pp. 2752–2759, 2020, doi: 10.1016/j.jeurceramsoc.2020.02.059.
[19] D. V. Vedel, P. V. Mazur, O. M. Grigoriev, L. M. Melakh, M. D. Bega, and Kozak I.V, "Obtaining and mechanical properties of high-entropy ceramics (TiZrHfNbTa)C (in Ukraine)," Journal of Superhard materials, vol. 5, pp. 1–10, 2022.
[20] L. Dakova et al., "Processing and Mechanical Properties of (Hf-Ta-Zr-Nb-Ti)C," Materials Science Forum, vol. 1082, pp. 84–89, Oct. 2023, doi: 10.4028/p-s8gm7c.
[30] Dmytro Vedel, Tamás Csanádi, Petro Mazur, Anton Osipov, Juraj Szabó, Vladyslav Shyvaniuk, Richard Sedlák, Oleksandr Stasiuk, Veronika Kuchárová, Oleg Grigoriev Effect of densification technology on the microstructure and mechanical properties of high-entropy (Ti, Zr, Hf, Nb, Ta) C ceramic-based cermets. Open Ceramics. Volume 19,2024